Hexagonal and roll flow patterns in temporally modulated Rayleigh-Bénard convection

Christopher W. Meyer, David S. Cannell, and Guenter Ahlers
Department of Physics, University of California, Santa Barbara, California 93106
and Center for Nonlinear Science, University of California, Santa Barbara, California 93106
(Received 27 November 1991)

We present experimental results for pattern formation in a thin fluid layer heated time periodically from below. They were obtained with computer-enhanced shadowgraph flow visualization and with heat-flux measurements. The experimental cell was cylindrical, with a radius-to-height ratio of 11.0. The temperature of the top plate was held constant while that of the bottom plate was modulated sinusoidally so that the reduced Rayleigh number $\epsilon \equiv \Delta T/\Delta T_c - 1$ had the form $\epsilon(t) = \epsilon_0 + \delta \sin(\omega t)$. Here the time t and frequency ω are scaled by the vertical thermal diffusion time. Experiments were performed within the ranges $8.0 \le \omega \le 18.0$, $0.4 \le \delta \le 3.3$, and $-0.2 \le \epsilon_0 \le 0.6$. Measurements of the convective threshold shift $\epsilon_c(\delta,\omega)$ were in good agreement with theoretical predictions. Comparisons were made with theoretical predictions of a range $\epsilon_A(\delta,\omega) \le \epsilon_0 < \epsilon_R(\delta,\omega)$ ($\epsilon_A < \epsilon_c, \epsilon_R > \epsilon_c$) where only a hexagonal pattern with downflow at the cell centers is predicted to be stable, a range $\epsilon_R \le \epsilon_0 < \epsilon_B(\delta,\omega)$ where both hexagonal and roll patterns are expected to be stable, and a range $\epsilon_0 \ge \epsilon_B$ where only a roll pattern should be stable. At low modulation amplitudes ($\delta \lesssim 1.2$ for $\omega = 15$) only rolls were observed over the range of ϵ_0 studied, although the rolls appeared perturbed for $\epsilon_A \le \epsilon_0 < \epsilon_R$. At moderately high amplitudes ($1.2 \lesssim \delta \lesssim 2.3$ for $\omega = 15$), a cellular pattern with local sixfold symmetry and downflow at the cell centers, which was reproducible from one cycle to the next, was observed over the range $\epsilon_A \lesssim \epsilon_0 \lesssim \epsilon_R$. Over the range $\epsilon_0 \gtrsim \epsilon_B$ roll-like patterns were observed. Over the range $\epsilon_R \lesssim \epsilon_0 \lesssim \epsilon_B$, where theory predicts bistability of rolls and hexagons, a coexistence between the two patterns was found. At high values of δ ($\delta \gtrsim 2.3$ for $\omega = 15$), a pattern consisting of randomly placed cells and short roll segments that was reproducible from one cycle to the next was observed in all three regions. At still higher values of δ ($\delta > 3.0$ for $\omega = 13$), this pattern was observed to be irreproducible from one cycle to the next. The transition from patterns resembling those predicted by the deterministic theory to irreproducible random patterns as δ is increased is presumed to be due to stochastic perturbations. These perturbations appear to play an important role in those parameter ranges where the amplitude of the pattern decays to a microscopic value during part of the modulation cycle.

PACS number(s): 47.25.Qv, 47.20.Bp, 47.20.Ky

I. INTRODUCTION

In a thin horizontal fluid layer heated from below, convection will occur when the temperature difference ΔT exceeds a critical value ΔT_c [1]. This phenomenon, which is known as Rayleigh-Bénard convection [2,3], is usually discussed in the approximation where the vertical temperature gradient in the conduction state is constant, and where all fluid properties are temperature independent except for the density where it enters into the buoyancy force. This approximation is known as the Oberbeck-Boussinesq (OB) approximation [4,5], and when it is applicable, the fluid flow which is stable immediately above the first instability in a laterally infinite system consists of straight rolls [6]. This flow pattern is particularly simple because upflow and downflow are equivalent in the sense that the original pattern can be recovered by reflection of the velocity field about the horizontal midplane of the sample (which corresponds to a reversal of the velocity everywhere), followed by horizontal translation of the pattern in the direction of the wave vector by half a wavelength. Whereas the OB fluid provides numerous interesting examples of pattern formation and bifurcation phenomena [7], the non-OB case has additional interesting features. These arise from the fact that upflow and downflow are no longer so simply related to each other because the fluid properties in the top and bottom part of the cell differ. Whereas the OB case allows only rolls as stable solutions, the stable pattern near onset for a non-OB fluid is one of hexagonal symmetry [8]. In the hexagons, upflow in the center and downflow near the outside of each cell is not equivalent to downflow in the center and upflow near the edges. Thus the original pattern cannot be recovered by a translation after a reversal of the velocity field. Whether the hexagons have upflow or downflow in the center is determined by the temperature dependence of the relevant properties of the system which determine the sign of a certain parameter $\mathcal{P}$ in the theory [8].

In the OB fluid, the rolls form via a forward or supercritical bifurcation when the Rayleigh number, which is proportional to ΔT, increases through its critical value R_c. By this we mean that the amplitude of the flow field grows continuously from zero as $\epsilon \equiv R/R_c - 1$ becomes positive. However, in the non-OB case, the hexagons form via a backward or subcritical bifurcation, i.e., the amplitude jumps discontinuously to a finite value as ϵ passes through zero quasistatically, and the bifurcation is

hysteretic. Figure 1 illustrates this, and shows schematically the stability ranges [8] of rolls and hexagons in the non-OB case. The amplitude A of the velocity field for rolls and for hexagons is shown as a function of ϵ. Dashed curves represent unstable solutions. The center of each hexagonal cell contains upflow (downflow) when A is positive (negative). The diagram assumes $\mathcal{P}>0$. Immediately above threshold, rolls, which appear through a supercritical bifurcation, are unstable to hexagons. They are stable for $\epsilon \geq \epsilon_R$. Hexagons are stable for $\epsilon_A \leq \epsilon \leq \epsilon_B$. For $\epsilon_R \leq \epsilon \leq \epsilon_B$ both hexagons and rolls are stable, and for the deterministic, laterally infinite, uniform system the pattern is expected to be determined by the past history. The hysteresis loop between ϵ_A and the threshold is extremely small. The size of these ranges increases with the deviation of the fluid layer from the OB approximation.

There are several ways of realizing a non-OB system. The straightforward one is to choose a fluid with strongly temperature-dependent properties and a sample thickness which leads to a large critical temperature difference ΔT_c. This case has been treated theoretically by numerous investigators [8–13], with the most complete treatment, considering the temperature variations of all relevant properties, being the one by Busse [8]. A number of relevant experiments have been performed over the years [14–20].

An alternate way of breaking the symmetry of the OB system is to subject the sample to internal heating. In that case the conduction temperature profile will be nonlinear, even though the fluid properties are essentially temperature independent. This also breaks the reflection symmetry about the midplane of the sample, and again hexagonal patterns occur. This case has been considered theoretically in some detail [13,21–23], but carefully controlled experiments are difficult and the results available so far [24] are only semiquantitative.

Another way of generating a nonlinear conduction profile is to subject the sample to time-dependent heating. This, too, will lead to an existence range of stable hexagons. The case where the heating consists of a temporal ramp of the top and bottom temperatures (keeping their difference constant) was treated both experimentally and theoretically by Krishnamurti, who found good agreement between her observations and calculations [25]. More recently, the temporal ramp was treated by Swift and Hohenberg as a special case of a theoretical model with arbitrary time dependence of the top and bottom temperatures [26]. Their results generally agreed with Krishnamurti's [27]. Clearly, the ramping experiment can be conducted only as a transient because the mean temperature changes monotonically.

An interesting variation of time-dependent heating experiments which leads to a nonlinear conduction profile and which lends itself to the study of *stationary* processes is the case of time-periodic modulation of the bottom- and/or top-plate temperature. In that case,

$$\epsilon(t)=\epsilon_0+\delta\cos(\omega t)\ . \tag{1.1}$$

The results of Fig. 1 are then still applicable, provided the amplitude A is replaced by its mean value and ϵ is replaced by ϵ_0. This case was examined theoretically [26,28–36] and experimentally [31,32,37–44] by several authors. Initially, however, the primary theoretical and experimental concern was the shift ϵ_c of the convective threshold which is predicted to occur in the presence of modulation, and no consideration was given to the interesting nonlinear effects which lead to the formation of a hexagonal pattern near the first bifurcation. Definitive experimental measurements of the threshold shift were made by Niemela and Donnelly [40], and their results agreed well with the theory [30,34–36]. Only fairly recently was it predicted by Roppo, Davis, and Rosenblat [33] that modulation should yield a stable range of hexagonal flow. A more quantitative treatment of the stability range of hexagons was provided by Hohenberg and Swift [26,35,36], who derived a 13-mode Lorenz model [45] which describes the relative stability of hexagons and rolls in the presence of modulation. It was also predicted [33,35] that the modulation of the bottom (top) plate should lead to downflow (upflow) in the centers of the cells. The only previous experiments on modulated convection which were done with flow visualization [41–44] were conducted at low modulation frequencies and amplitudes where the range of stability of hexagons is unobservably small.

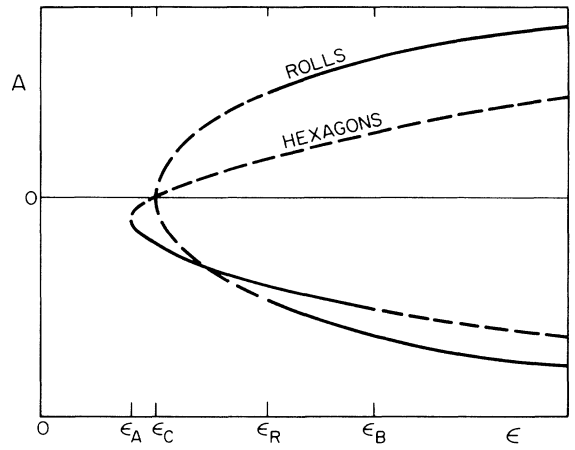

FIG. 1. Bifurcation diagram for non-Oberbeck-Boussinesq (non-OB) convection, showing the convective amplitude A as a function of the reduced Rayleigh number ϵ. The dashed lines represent unstable solutions. Hexagonal flow occurs through a subcritical bifurcation and is stable for $\epsilon_A \leq \epsilon \leq \epsilon_B$. The flow in the center of each hexagon is upwards for $A>0$, and downwards for $A<0$. This diagram represents a non-OB fluid layer with a positive value of $\mathcal{P}$ (see text). For a layer with negative $\mathcal{P}$ the hexagonal solution is inverted about the ϵ axis. The bifurcation to rolls is supercritical, but rolls are stable only above ϵ_R.

In the present paper we report experimental studies of the effect of bottom-plate temperature modulation on the convective pattern and on heat flow in a parameter range where hexagons have a significant range of stability. We compare our results with an appropriate special case of the 13-mode Lorenz model of Hohenberg and Swift [35]. Whereas we find generally good agreement, there are phenomena which occur in the experiment and which have not been considered in the theory. The model as-

sumes a spatially uniform pattern consisting either of hexagons or of rolls. In the experiment we find that the two coexist in the range of multistability where either is stable. This observation differs from the ordinary non-OB case where the temperature difference is steady, and where essentially only one phase exists because the transition from hexagons to rolls (rolls to hexagons) occurs when the rolls (hexagons) acquire a lower generalized potential [19,20]. The hexagons produced by the modulation, being a time-periodic state, cannot be described by a potential, and the reason for the coexistence may be associated with that. On the other hand, it is possible that the coexistence is the result of stochastic forces which can have a significant influence when the pattern amplitude becomes microscopic during part of the modulation cycle. We also find a parameter range involving large modulation amplitudes where the pattern is neither hexagonal nor roll-like, but instead consists of randomly arranged cellular flow which is irreproducible from one modulation cycle to the next. We believe that this phenomenon is related to the stochastically induced patterns which we have reported elsewhere [42,43,46] for much smaller modulation frequencies and for temporal ramps of ϵ.

Brief reports on this work have already been presented elsewhere [41,47,48].

The remainder of this paper is organized as follows. In Sec. II we briefly review the predictions of the 13-mode Lorenz model of Hohenberg and Swift. We present numerical results based on a nine-mode special case of that model in the parameter ranges of our experiments. Section III presents a description of our apparatus, and of the experimental methods which were used. The results of this work are given in Sec. IV. In Sec. V we provide a summary.

II. THEORETICAL PREDICTIONS

The prediction that a hexagonal pattern could be stabilized in Rayleigh-Bénard convection by subjecting the temperature difference across the cell to external temporal modulation was made by Roppo, Davis, and Rosenblat [33]. Their theory, however, involved a perturbation expansion in the modulation amplitude δ, whose validity was shown [35] to be limited to the range $\delta/\omega \lesssim 0.06$ where the range of hexagons is unobservably small. Recently, Hohenberg and Swift (hereafter referred to as HS) derived [35] a 13-mode Lorenz model [45] which confirmed the qualitative prediction of Roppo, Davis, and Rosenblat, but which was not limited to small values of δ. A conclusion of HS was that there is an optimal frequency range for observing hexagons, since their stability region vanishes not only for $\omega \to \infty$, but also for $\omega \to 0$.

The Lorenz model [45], which assumes a laterally infinite layer and a spatially homogeneous pattern, involves a truncation of an expansion of the solutions to the equations of motion [Eqs. (2.2a)–(2.2c) of HS]. It was derived for the case of modulated convection by Ahlers, Hohenberg, and Lücke [32,34], and involves $\epsilon(t)$ as given by Eq. (1.1) as a parameter. Their three-mode model, however, assumes a straight-roll pattern and does not allow for competition between rolls and hexagons. HS showed that this competition can be described by the addition of extra modes. They arrived at a 13-mode model [26,35] representing three sets of rolls oriented at angles of $2\pi/3$ to each other, and the nonlinear interactions between them. The superposition of the rolls leads to a hexagonal pattern when all three have equal amplitudes, and to a roll pattern when the amplitudes of two sets vanish. HS simplified their model by imposing the restriction, valid for stationary solutions, that two of the rolls have equal amplitudes. This leads to a nine-mode model consisting of the eight amplitudes x_{nR}, y_{nR}, x_{nH}, y_{nH}, $n=1,2$, and an amplitude z which is of quadratic order and is related to the convective heat current j^{conv} by

$$j^{\text{conv}}=g^{-1}z \ . \tag{2.1}$$

Here the coefficient g can be calculated for the laterally infinite system [6,36], but for the finite system it is best taken from experiment in the absence of modulation [46]. The mode amplitudes x_{nR} and y_{nR} give the amplitudes of the lowest velocity and temperature mode, respectively, of a roll pattern, and x_{nH} and y_{nH} do the same for the hexagonal pattern. When the amplitude x_{1H} is positive (negative), the solution of the model corresponds to hexagons with upflow (downflow) in the center. The nine-mode model is given by Eqs. (2.10) and (2.12) of HS, and will not be reproduced here. Although HS solved their model analytically for various limiting cases, none of these solutions are applicable in the parameter range accessible to our experiment. We therefore integrated the equations numerically in order to obtain theoretical predictions for the stability ranges of hexagons and rolls suitable for comparison with our measurements.

The diagram of Fig. 1 is made applicable to modulated convention [33] by changing the ordinate from A to the average $\overline{A}$ of A over the modulation cycle, and the abscissa from ϵ to $\epsilon_0-\epsilon_c$ where ϵ_c is the shift in the convective threshold due to the modulation. One can further make the identification $\overline{A}=x_{1R}$ for rolls, and $\overline{A}=x_{1H}$ for hexagons. We caution the reader that the definitions of ϵ_A, ϵ_R, and ϵ_B used in this paper differ from those used by HS by the additive constant ϵ_c.

For the numerical results to be presented we used a Prandtl number $\sigma=3.6$ corresponding to our experiments, and took g from static measurements for our cell.

The effect of external modulation on $j^{\text{conv}}=\overline{z}/g$ is illustrated in Fig. 2(a). The case of steady heating is given by the dashed curve. The solid curves correspond to modulation with $\delta=2.0$ and $\omega=15$. For steady heating, $j^{\text{conv}}=0$ for $\epsilon_0 \le 0$. Above threshold, j^{conv} increases linearly with ϵ_0 such that $j^{\text{conv}}=g^{-1}\epsilon_0$. The pattern consists of rolls. Under modulation the threshold is shifted to $\epsilon_c=0.1378$. Figure 2(b) provides a closeup view of the hysteretic bifurcation. When ϵ_0 is continuously increased from zero, j^{conv} has a value of zero until ϵ_c is reached, at which point j^{conv} jumps to a finite value on the hexagon solution. The hexagons remain stable as ϵ_0 is decreased until $\epsilon_0=\epsilon_A=0.1362$, where j^{conv} jumps to zero. This hysteresis loop is very small; $\epsilon_c-\epsilon_A=0.0016$. With the stability of our apparatus (ϵ_0 may drift by as much as

0.003), such a small loop is not observable.

The larger hysteresis loop between ϵ_R and ϵ_B is shown in Fig. 2(c). In this case, the range of the loop is $\epsilon_B - \epsilon_R = 0.104$, which is almost two orders of magnitude larger than the loop between ϵ_A and ϵ_c, and is easy to resolve experimentally. As ϵ_0 is increased from ϵ_c, the system remains on the hexagon solution until ϵ_B, at which point j^{conv} jumps up to its value on the roll solution. If, at that point, ϵ_0 is decreased, the system stays on the roll branch until $\epsilon_0 = \epsilon_R$, where it jumps to the hexagon solution.

We determined the stability boundaries ϵ_c, ϵ_R, and ϵ_B for given values of δ and ω by numerically integrating the HS nine-mode model and examining the growth rate from one cycle to the next of $|x_{1R}|$ and $|x_{1H}|$ once initial transients had died away. The value of ϵ_c was found by assigning the initial condition $x_{1R} = x_{1H} = -10^{-6}$. We defined ϵ_c to be the point where the growth rate of $|x_{1R}|$ was zero. For $\epsilon_0 < \epsilon_c$ the growth rate was negative, and for $\epsilon_0 > \epsilon_c$ it was positive. We determined ϵ_R by assigning the initial values $x_{1H} = -10^{-6}$ and $x_{1R} = -10^{-1}$. Then ϵ_R was defined to be the point where the growth

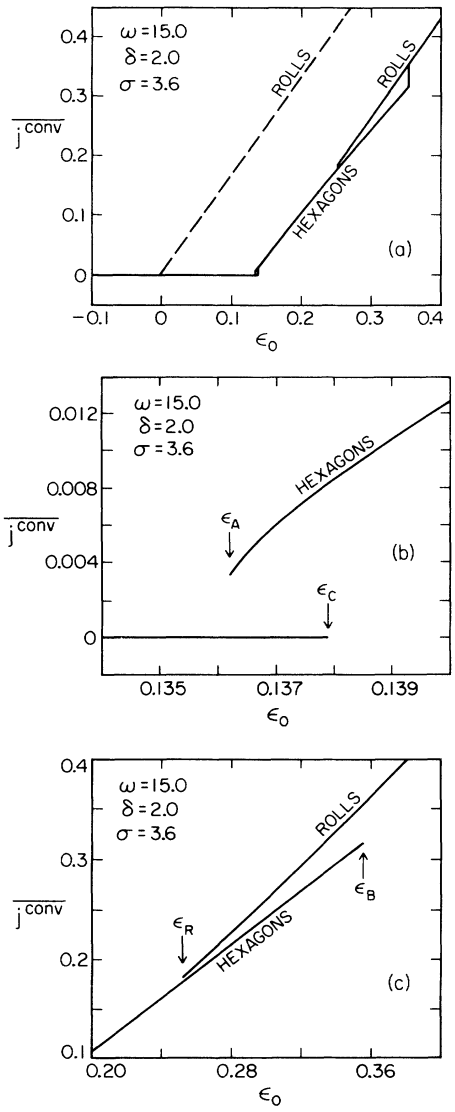

FIG. 2. (a) Prediction of the Hohenberg-Swift (HS) nine-mode Lorenz model (see Ref. [35]) for the convective heat current averaged over one modulation cycle $\overline{j^{\text{conv}}}$ as a function of ϵ_0 (the mean value of ϵ) for modulations with amplitude $\delta = 2.0$ and frequency $\omega = 15$ (solid curves). The Prandtl number used in the model is $\sigma = 3.6$, which corresponds to that of the fluid used in the experiments. The dashed line represents $j^{\text{conv}}(\epsilon)$ for a steady heat current. Modulation shifts the convective threshold from $\epsilon_0 = 0$ to $\epsilon_0 = \epsilon_c$. Hexagons are stable for $\epsilon_A \leq \epsilon_0 \leq \epsilon_B$, and rolls are stable only above ϵ_R. (b) Closeup of the hysteretic loop between ϵ_A and ϵ_c. (c) Closeup of the hysteretic loop between ϵ_R and ϵ_B. Note that the definitions of ϵ_A, ϵ_R, and ϵ_B used here differ from those of HS by the overall additive constant ϵ_c.

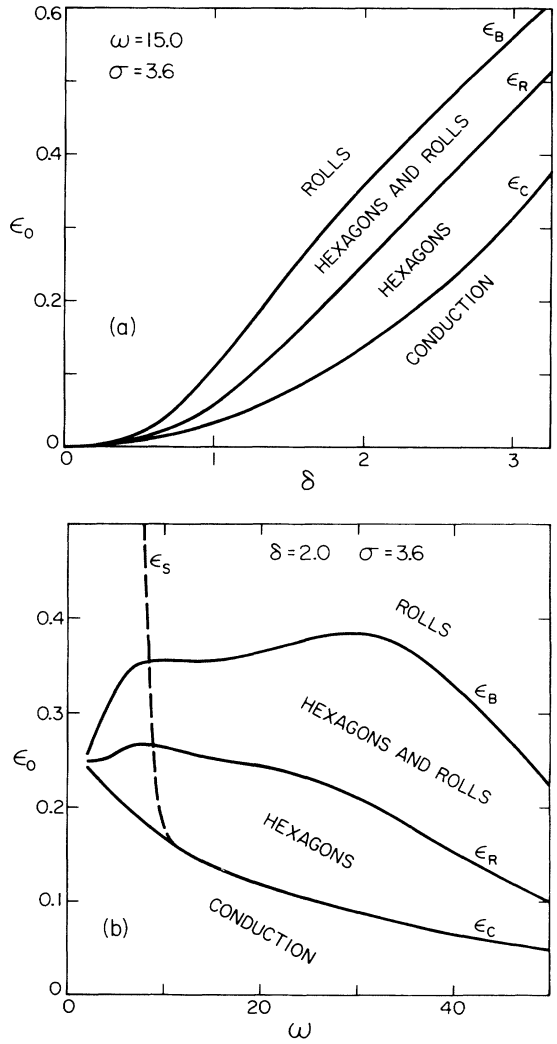

FIG. 3. (a) Stability limits of hexagons and rolls in the $\epsilon_0 - \delta$ plane for modulated convection with $\omega = 15$ and $\sigma = 3.6$. The curves show the predictions of the HS model for ϵ_c, ϵ_R, and ϵ_B. (b) Stability limits in the $\epsilon_0 - \omega$ plane for $\delta = 2.0$ and $\sigma = 3.6$. The solid curves show the HS predictions for ϵ_c, ϵ_R, and ϵ_B. The dashed line corresponds to the condition $j^{\text{conv}}(t) \leq 1.25 \times 10^{-6}$. Patterns modulated at small ω ($\omega \leq 1$) exhibited stochastic cellular flow when $j^{\text{conv}}(t)$ fell below this value during the modulation cycle [42].

rate of $|\overline{x_{1H}}|$ was zero. For $\epsilon_0 < \epsilon_R$ this growth rate was positive, and for $\epsilon_0 > \epsilon_R$ it was negative. Finally, for determining ϵ_B, the initial values assigned were $x_{1H} = -10^{-1}$, $x_{1R} = -10^{-6}$, and ϵ_B was defined to be the point where the growth rate of $|\overline{x_{1R}}|$ was zero. For $\epsilon_0 < \epsilon_B$ the growth rate was negative, and for $\epsilon_0 > \epsilon_B$ it was positive. Note that the signs of the initial values of x_{1H} and x_{1R} were chosen to be negative. While the choice for the sign of the initial value of x_{1R} was arbitrary, that for x_{1H} was not, because the sign of x_{1H} determines the flow direction in the centers of the hexagons. When x_{1H} was given a positive initial value it was always found to decay with time.

Shown in Fig. 3(a) is a plot of ϵ_c, ϵ_R, and ϵ_B as a function of δ for $\omega = 15$. For $\delta < 1$ the range of ϵ where hexagons are stable is very small, making them difficult to observe. At larger values of δ, the range becomes considerably larger and observation of the hexagons becomes feasible. Figure 3(b) shows ϵ_c, ϵ_R, and ϵ_B as a function of ω for $\delta = 2.0$. The range where hexagons are stable is very small at low frequencies, but it rises rapidly to reach an observable value for $\omega \gtrsim 10$. The maximum value of $\epsilon_R - \epsilon_c$ is found at $\omega \approx 25$, and that for $\epsilon_B - \epsilon_c$ is found at $\omega \approx 30$. At higher frequencies both $\epsilon_R - \epsilon_c$ and $\epsilon_B - \epsilon_c$ decrease monotonically towards zero. Most experiments described in this paper were performed with modulation parameters represented within these two plots.

The results we have presented will change when the Prandtl number is changed. Further, it is important to note that since the HS model involves a truncation of the solutions to the equations of motion, its predictions are not expected to be accurate for all values of δ, ω, and ϵ_0. Its predictions have been shown [35] to be exact in the limit $\delta \ll \omega/2\pi^2 \ll 1$. HS have also shown, by comparing the results of the model with exact predictions in certain other limiting cases, that near threshold the model is accurate to within 15%. The values of δ and ω used in our experiments, however, do not correspond to these limiting cases, so it is not clear *a priori* how accurate the model predictions should be for the parameters that we used.

III. APPARATUS AND EXPERIMENTAL METHODS

A. The fluid

The fluid used was water near 50.6 °C. It had thermal conductivity $\Lambda = 6.41 \times 10^{-3}$ W/cm K, thermal diffusivity $\kappa = 1.52 \times 10^{-3}$ cm^2/s, and kinematic viscosity $\nu = 5.50 \times 10^{-3}$ cm^2/s. This leads to a Prandtl number $\sigma \equiv \nu/\kappa = 3.6$. The water was distilled and fed through a Milli-Q ion-exchange system (Millipore Co.) to achieve high purity. It was degassed by boiling before it was placed in the cell. The fluid layer was $d = 0.35$ cm thick, resulting in a predicted critical temperature difference $\Delta T_c = 0.735$ °C and a vertical thermal diffusion time $t_v \equiv d^2/\kappa = 80.6$ s. When $\Delta T = 4.5 \Delta T_c$ [$\Delta T(t)$ never exceeded this value during the experiments] in such a layer, the parameter $\mathcal{P}$ which describes the extent of the departure from the OB approximation [8] has a value of $\mathcal{P} = -0.298$. For this value of $\mathcal{P}$ and steady heating a pattern of rolls is predicted [8] to be unstable to hexagons only over the small range $0 \leq \epsilon \leq 1.02 \times 10^{-3}$. Experimentally we never detected a hexagon pattern immediately above threshold without modulation, and we believe that this system conforms very well to the OB approximation.

B. The apparatus

A special apparatus was designed for the purpose of achieving high-amplitude modulations of the temperature of the bottom plate. A schematic diagram is shown in Fig. 4. It consisted of a cell whose top plate was in contact with flowing temperature-controlled water and whose bottom plate was also in contact with flowing, but separately controlled, water. The water in contact with the top plate was held at 50.6 °C, and that in contact with the bottom plate was held at 14.3 °C. While the upper surface of the top plate was held at the temperature of the top bath, the temperature of the *bottom* plate was raised close to that of the *top* bath by a heater embedded in the bottom plate. A large power (≈ 90 W) was needed for this, and this heat flowed primarily into the bottom bath and not through the sample. By modulating this power about its mean value, substantial modulation of the temperature of the bottom plate could be achieved.

The top plate was a single-crystal sapphire disk with a diameter of 10.16 cm and a thickness of 0.318 cm. The plate was flat to within 5 μm. The bottom plate was a composite of three disks which were epoxied (Stycast 1266) together. A schematic diagram is shown in Fig. 5. The top disk was made of copper and had a diameter of 8.9 cm and a thickness of 0.48 cm. It was plated on its upper side with 0.015 cm of nickel which was lapped and polished to provide a mirror surface which was flat to within 2 μm. A small groove, 2 mm wide and 0.7 mm deep, was machined into the bottom of the disk as shown. A second groove, which was 3 mm wide, 2 mm deep, and 1 cm long was located at the end of the groove; a small thermistor (Fenwell GA51SM2) was epoxied (Stycast 2850 FT) in this second groove for measuring the temperature of the disk. The leads of the thermistor exited the disk through the first groove. The central disk of the bottom plate, which was also made of copper, was 8.6 cm in diameter and 0.32 cm thick. An array of 26 parallel grooves, 1 mm wide, 0.5 mm deep, and separated by 3.2 mm, was machined into the bottom of this disk. Also machined into that side was a concentric groove of the same dimensions located at a radius of 4.5 cm. It connected all of the parallel grooves. Within these grooves was placed 1.73 m of 0.25-mm-diam manganin wire with a resistance of 16.2 Ω which was used as the bottom-plate heater. The wire was coated with a thin layer of varnish and epoxied (Stycast 2850 FT) into the grooves. The bottom disk, which was made of acrylic, was 8.6 cm in diameter and 0.4 mm thick. Its purpose was to electrically insulate the heater from the flowing water, and to provide some thermal resistance between the water and the bottom plate. The thermal resistance allowed the plate to warm up when power was applied to the heater. A 0.8-mm-diam vertical hole, located 3.2 mm from the outer

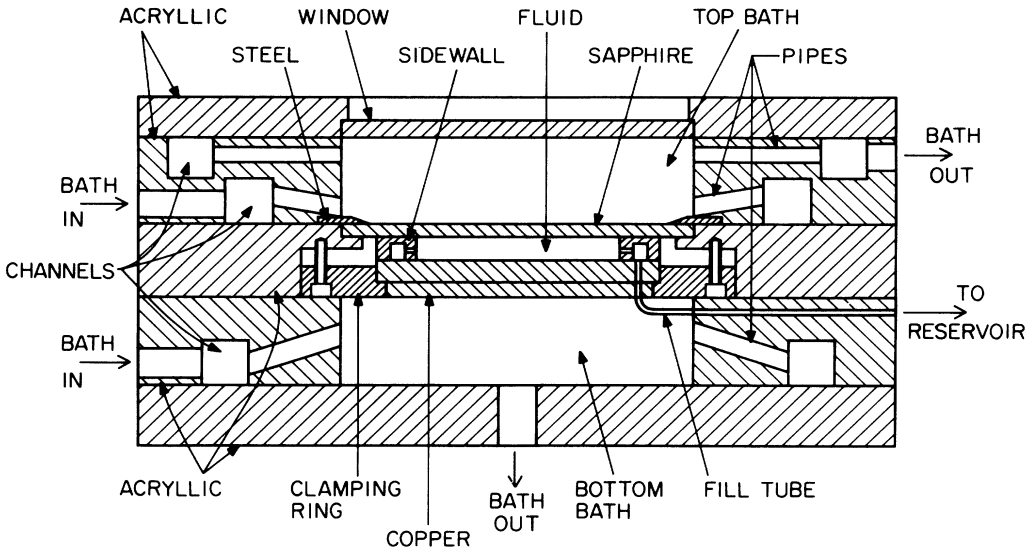

FIG. 4. Schematic diagram of the apparatus.

edge of the top disk, was drilled through the entire bottom plate to provide an outlet for the water to allow for thermal expansion. This fillhole was connected on the bottom side of the plate to a plastic tube which exited the apparatus and was connected to a reservoir of pure water.

Two bottom plates, differing in the design of the thermistor-lead groove, were used. Schematic diagrams of the two designs are shown in Fig. 5(b), which provides top views of the plates. In plate A the groove lay on a diameter and was 6.0 cm long. In plate B the groove was circular at a radius of 4.0 cm for about 180° before exiting as shown.

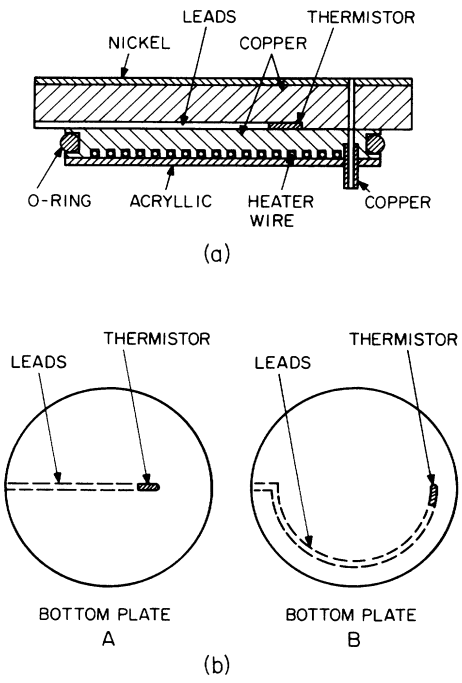

FIG. 5. Schematic diagram of the bottom plate of the convection cell. (a) Cross-sectional view. (b) Top view of bottom plates A and B, illustrating the locations of the thermistor probes and their leads.

Two sidewall designs were used with the apparatus, as shown in Fig. 6. The first sidewall (A) was made of Delrin (acetal homopolymer), while the second one (B) was made of acrylic. Both were cylindrical, with an outer diameter of 8.9 cm, and were sealed with 1.1-mm-diam *O* rings, as shown. Their inner diameter was 7.7 cm, yielding an aspect ratio $L = 11.0$. A small channel of height 1.3 mm and width 2.5 mm was located in the lower surface of each sidewall. The fillhole in the bottom plate was located beneath the channel. In sidewall A the wall separating the cell from the channel was raised by ≈ 0.10 mm to allow the fluid to flow between the cell and the channel. In sidewall B the fluid flowed instead through 80 horizontal radially directed holes of 0.3 mm diameter. These holes were located at the midheight of the cell and were evenly distributed azimuthally. This design kept the large flow velocities that occur in the vicinity of the fillhole as the fluid expands and contracts under time-dependent heating out of the convecting portion of the cell. Previous experience (see Fig. 2 of Ref. [46]) had shown that these large flow velocities forced convective flow patterns of concentric rolls centered around the fillhole.

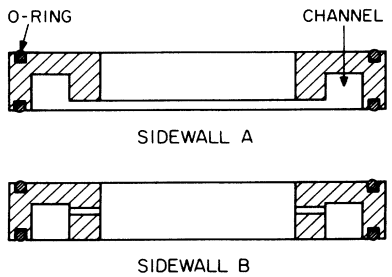

FIG. 6. Schematic diagram of the two sidewall designs.

As illustrated in Fig. 4, the top plate of the cell was mounted in a 1.5-cm-thick acrylic disk with a diameter of 25.4 cm, which we shall call the "cell container disk." The top plate was held in place by a stainless steel ring as illustrated. This ring had an inner diameter of 9.4 cm, outer diameter of 12.5 cm, and thickness of 1.6 mm. An acrylic ring was used to clamp the cell together through the use of six machine screws as shown in the figure.

An acrylic flow-distributor ring of outer diameter 25.4 cm, inner diameter 10.2 cm, and thickness 2.54 cm was mounted above the cell container disk. This ring was used to circulate temperature-controlled water at a rate of about 200 ml/s above the top plate of the cell, maintaining it at 50.6 °C. The water entered the region above the top plate by way of 24 holes of diameter 5 mm. The holes were directed radially inward and pointed slightly downward in order to direct the water onto the top plate at a distance of about 2.25 cm from the center. They were evenly distributed around the ring and were connected by an azimuthal channel of height 1 cm and width 1.5 cm, located in the bottom side of the ring at a radius $r=8.7$ cm. Water entered this channel from a circulating source outside the apparatus. The water exited through 24 horizontal holes of diameter 5 mm located directly above the inlet holes. The water flowed through these holes into a second azimuthal channel with the same dimensions as the first, and then exited the apparatus. A 10-cm-diam glass window, through which the inside of the convection cell could be observed, was mounted in the center of an acrylic plate of diameter 25.4 cm and thickness 1.2 cm, as shown.

A second acrylic flow-distributor ring with the same dimensions as the first was mounted below the cell container disk. Circulating water at 14.3 °C entered the region below the bottom plate by means of a flow-distribution system similar to that described above. The water exited the apparatus through a central hole in an acrylic disk of diameter 25.4 cm and thickness 1.9 cm, as shown.

The flow-distribution system provided efficient removal of the heat flowing through the cell. Despite this, the temperature of the top plate of the cell increased slightly when a sufficiently high heat current passed through it. Therefore a thermistor probe (Fenwell GA51M2) was placed in the bath resting on the top of the top plate in order to measure its temperature. Normally it was located directly above the sidewalls of the cell so as not to interfere with flow visualization, but it was moved across the top of the top plate at other times in order to measure possible horizontal temperature variations. When the steady-state temperature difference between the bottom and top plates was approximately equal to its convective onset value, temperature variations of 2×10^{-3} °C were measured across the diameter of the top plate. The temperature was lowest at a radius of about 2.25 cm, and increased with larger and smaller r.

All experiments were automated with a PC-XT computer which controlled the time-periodic power applied to the heater in the bottom plate, measured the temperatures of the bottom and top plates, and caused shadowgraph images of the flow patterns to be taken.

C. Pattern measurements and analysis

We used a computer-interfaced shadowgraph method to acquire digital images of the flow patterns. A detailed description of the necessary apparatus and of the image processing is given elsewhere [46]. The method yields images in which regions of downflow (upflow) are relatively bright (dark). The rapid emergence and disappearance of a pattern observed during a modulation cycle at the relatively high frequencies of the present work prevented averaging a large number of images to improve the signal-to-noise ratio. However, much of the noise could be eliminated by filtering techniques [46].

We determined the average wave number $\bar{k}=\int\int |k| I(k) dk_x dk_y$ of the pattern, where $I(k)$ is the normalized magnitude of the Fourier transform of the image. We also calculated the standard deviation σ_k of k from $\bar{k}$. A more detailed description of this analysis is given in Ref. [46]. The measurements of $\bar{k}$ and σ_k were scaled by dividing them by $k_c=3.117$.

Another quantity used to characterize a pattern was the total length B of the boundary separating regions of upflow and downflow [46], which provided a measure of the cellularity of the pattern. The value of B was normalized [46] by a factor involving $\bar{k}$ in such a way that a straight-roll pattern with arbitrary k would have $B=1$. The boundary length of a hexagon pattern is larger (typically by 20%).

D. Heat-flux measurements

The temperature difference ΔT across the cell was directly measured with the thermistors inside the bottom plate and above the top plate. At the operating temperature of 50.6 °C the sapphire top plate had a conductivity of $\Lambda=0.32$ W/cm K, which is 50 times that of water at 50.6 °C, and had a thickness that was 0.91 times that of the fluid layer. The plate therefore had a temperature difference that was 1.8% of the total measured ΔT. Further, for a nonzero heat current a small temperature difference existed between the top of the plate and the top bath; this temperature difference was carried across a boundary layer of thickness ≈ 1 mm in the bath immediately above the plate. The temperature measured by the probe, whose head was also ≈ 1 mm in diameter, was a spatial average over that in the boundary layer. Because of these additions to the true temperature difference across the fluid layer, measurements of ΔT were systematically too large by 2–3 %.

The heat current through the fluid was not directly measurable. Instead the total heat current $\dot{Q}$ generated in the bottom-plate heater was accurately controlled, and the temperature difference ΔT was measured. For $\Delta T=0$ no heat flowed through the cell, but a current $\dot{Q}_0$ of about 90 W flowed from the bottom plate into the 14.3 °C circulating water. In steady-state conditions with no convection, the total heat current was purely conductive and given by

$$\dot{Q}-\dot{Q}_0\equiv\dot{Q}^{\rm cond}=\Lambda_f A_f \Delta T/d+G\Delta T\ , \tag{3.1}$$

where A_f, Λ_f, and d are the cross-sectional area of the

fluid layer, its thermal conductivity, and thickness, respectively, and where G is the thermal conductance parallel to the fluid in the cell. We determined G from measurements of $\dot{Q}$, $\dot{Q}_0$, and ΔT for $\Delta T < \Delta T_c$, using values of Λ_f corresponding to the average temperature of the fluid. For steady-state conditions, the convective heat current $\dot{Q}^{\rm conv}$ is simply

$$\dot{Q}^{\rm conv} \equiv \dot{Q} - \dot{Q}_0 - \dot{Q}^{\rm cond} . \tag{3.2}$$

The dimensionless heat-current density $j^{\rm conv}$ is the ratio of $\dot{Q}^{\rm conv}$ to the heat conducted through the fluid at $\Delta T = \Delta T_c$. The Nusselt number N is the ratio of the total heat current through the fluid to that which would be conducted by a motionless fluid under the same conditions, and is thus related to $j^{\rm conv}$ by

$$j^{\rm conv} = (N-1)(1+\epsilon) . \tag{3.3}$$

New static heat-flux measurements were made whenever the cell had been taken apart. They were very similar to those shown in Fig. 5 of Ref. [46]. As was experienced there [46], the values of ΔT_c typically varied by 1–2 %, although for a given cell assembly they were reproducible to 0.1% or so. A typical value of ΔT_c was 0.726 °C, which is within 1% of the theoretical value for a laterally infinite system with perfectly conducting top and bottom plates. After correction for the temperature difference across the sapphire, the initial slope of $N(\epsilon)$ gave $g = 0.79$, which does not differ significantly from the values obtained in Ref. [46]. Results for g varied typically by 1–2 % between successive cell assemblies.

IV. RESULTS

A. Heat-flux measurements

Here we present measurements of the convective heat current averaged over a modulation cycle $j^{\rm conv}$ as a function of ϵ_0. They yield information on the convective threshold shift, and on the initial slope of $\overline{j^{\rm conv}}(\epsilon_0)$ above the threshold. Similar measurements were made by Niemela and Donnelly [40] in experiments with liquid helium with $\sigma = 0.49$, and yielded the first experimental confirmation of the theoretically predicted [28–30,32,34,35] threshold shift.

All heat-flux measurements were taken using bottom plate A and sidewall B. Shown in Fig. 7 are results for $\omega = 15$ and $\delta = 1.97$. They were obtained by beginning the experimental run with $\epsilon_0 \approx -0.1$ and modulating for 40 cycles at each value of ϵ_0. Measurements were made of $\Delta T(t)$ and $\dot{Q}(t)$ during the last 36 cycles. By incrementing $\bar{Q}$, ϵ_0 was increased by approximately 0.02 and a new 40-cycle set was performed. This procedure continued until $\epsilon_0 \approx 0.5$. The results in Fig. 7 show a threshold shift of over 10%, with a somewhat rounded bifurcation. This rounding is due to the modulation; in the absence of modulation the bifurcation was as sharp as that shown in Ref. [46], Fig. 5. Above $\epsilon_0 = 0.15$, $j^{\rm conv}$ increases linearly within our resolution. We determined the threshold shift and initial slope by calculating the best-fit line through the points above $\epsilon_0 = 0.15$. The line shown in Fig. 7 is this fit.

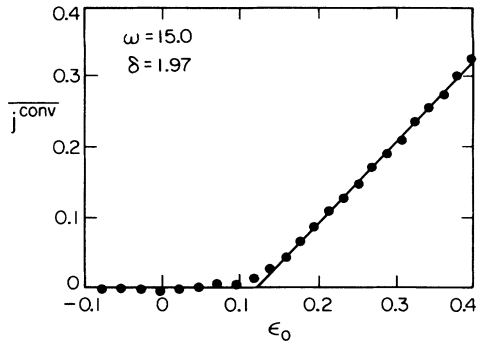

FIG. 7. Measurements of $\overline{j^{\rm conv}}$ for an experimental run with $\omega = 15$ and $\delta = 1.97$. The line is a fit to the points for $\epsilon_0 > 0.15$, where the increase of $\overline{j^{\rm conv}}$ is linear. It gives ϵ_c and the initial slope S_i of $\overline{j^{\rm conv}}$.

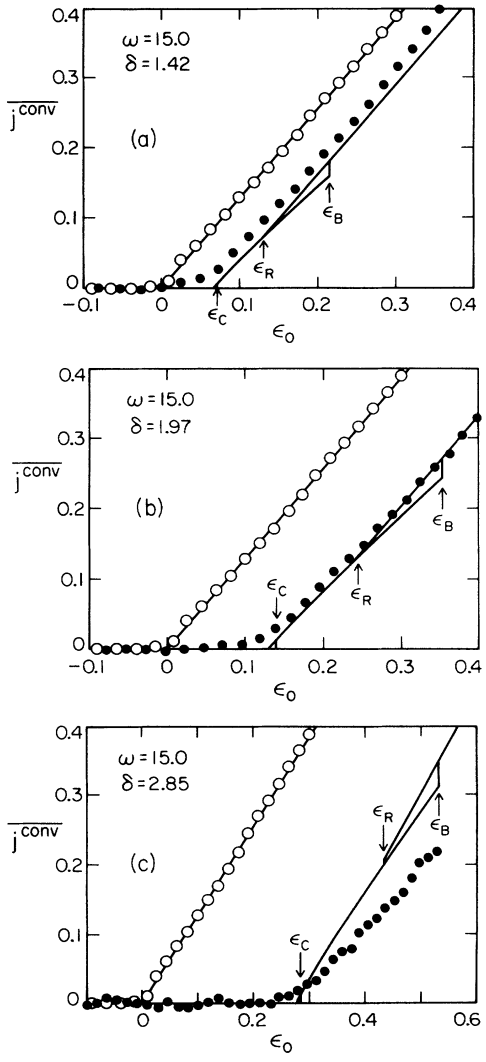

FIG. 8. Comparison of experimental measurements (shown as solid circles) of $\overline{j^{\rm conv}}(\epsilon_0)$ with the predictions of the nine-mode model. The open circles are from static measurements ($\delta = 0$). The solid curves are the predictions. Only stable states are shown. Note the small hysteretic loop immediately below ϵ_c, which is visible in (b).

Shown in Fig. 8 as solid circles are measurements taken as described above and also for $\omega=15$. They are for (a) $\delta=1.42$, (b) $\delta=1.97$ (the same as in Fig. 7), and (c) $\delta=2.85$. The open circles are measurements without modulation. The best-fit line through the static measurements was used to determine the unshifted threshold $\Delta T_c(\omega=0)$. The initial slope for the static measurements was $S_i=1.28$, corresponding to $g=0.781$. The threshold shifts were (a) $\epsilon_c=0.052$, (b) $\epsilon_c=0.122$, and (c) $\epsilon_c=0.265$. The initial slopes in Figs. 8(a), 8(b), and 8(c) were $S_i=1.22$, 1.16, and 0.83, respectively.

Predictions of j^{conv} for the experimental runs from the HS Lorenz model are shown in Fig. 8 as solid curves. Here we used Eq. (2.1), with $g^{-1}=S_i(\omega=0)$, and $S_i(\omega=0)=1.28$ taken from the static experiment. The locations of the theoretical values for ϵ_c, ϵ_R, and ϵ_B are indicated by the arrows. The predictions for ϵ_c are 0.070, 0.138, and 0.283 for Figs. 8(a), 8(b), and 8(c), respectively, in good agreement with the experimental measurements. Although ϵ_A is not indicated by arrows in Fig. 8, the hysteresis loop between ϵ_A and ϵ_c is shown. It is barely noticeable on the scale of the figure, however. The experimental heat-flux values show no evidence of a discontinuous jump at ϵ_c because the jump is masked by the rounding of the bifurcation. Even though the model predicts that rolls should not occur until $\epsilon_0>\epsilon_B$, heat-flux predictions for a roll pattern (upper curve) as well as a hexagonal pattern (lower curve) are shown in Fig. 8 for $\epsilon_R\leq\epsilon_0\leq\epsilon_B$. The measurements do not exhibit the discontinuity of j^{conv} at ϵ_B which is predicted by the model, nor do they show any type of change at this point. To investigate this further, we performed a run similar to those described above, but with ϵ_0 starting at ≈ 0.4 and *decreasing* after each set of 40 modulation cycles until it reached a value of -0.1. We found that within experimental resolution measurements with increasing and decreasing ϵ_0 agreed with each other. Despite the lack of qualitative agreement between experiment and the model at $\epsilon_0\approx\epsilon_B$, the measured heat-flux values in Figs. 8(a) and 8(b) are in good overall agreement with their corresponding theoretical predictions. The same cannot be said for those of Fig. 8(c), where the measured values fall significantly below those predicted by the model.

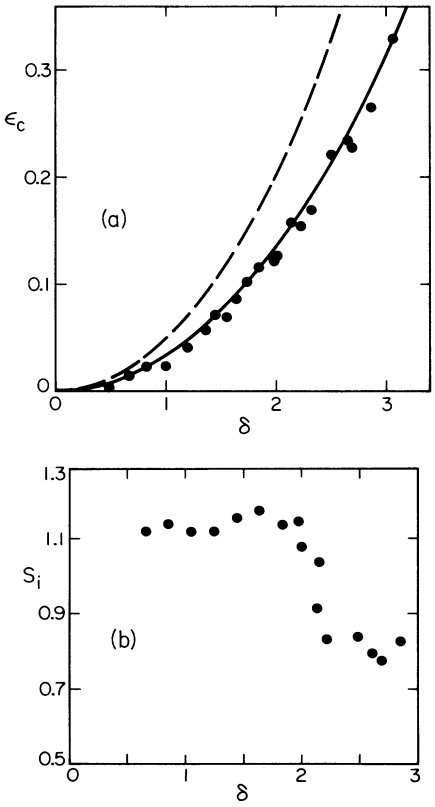

FIG. 9. (a) Experimental values of ϵ_c as a function of δ for $\omega=15$ (shown as circles). The solid curve represents the prediction of the nine-mode model, while the dashed curve shows that of the three-mode model of Ahlers, Hohenberg, and Lücke (see Ref. [34]). (b) The initial slope S_i of j^{conv} above the convective threshold as a function of δ for $\omega=15$.

Shown in Fig. 9(a) are the experimental measurements of ϵ_c as a function of δ for $\omega=15$. The measurements were made in the same manner as those shown in Fig. 7. The solid curve represents the predictions of the HS nine-mode Lorenz model, while the dashed curve represents those of the three-mode Lorenz model of Ahlers, Hohenberg, and Lücke [34]. Although the experimental points systematically fall slightly below the curve of the nine-mode model, the agreement is nevertheless quite impressive. The predictions of the three-mode model, however, deviate considerably from the experimental measurements. The difference between the predictions is due to the larger number of modes in the HS model, which gives it higher accuracy. At a lower frequency ($\omega=10$) it was found [40] that the three-mode model made very accurate predictions of the threshold shift. It is not as accurate at $\omega=15$ because the importance of the higher-order modes increases with frequency [34].

The initial slope of j^{conv} above the convective threshold is shown as a function of δ for $\omega=15$ in Fig. 9(b). These results were taken from the same experimental runs used to determine ϵ_c. For $0.5\leq\delta\leq 2.0$ they are roughly constant at a value of $S_i\approx 1.15$, which is 10% lower than S_i^{stat}. Above $\delta=2.0$, however, S_i drops substantially to a value ≈ 0.8. Due to the large scatter in the data it is not clear whether the decrease is sudden or smooth. In order to understand the reason for the behavior of S_i it is of course important to be able to observe the convective pattern. We will therefore defer discussion of this behavior until Sec. IV F, where we will examine the patterns corresponding to the heat-flux measurements of Fig. 8(c).

B. Initial survey of the parameter space

In the experimental runs described in Sec. IV A, the pattern faded away and later reappeared essentially unchanged during the course of each cycle. Images were taken during the 40th cycle at each value of ϵ_0, at the time when the intensity was approximately at its peak. In Fig. 10 images are shown for $\omega=15$ and $\delta=2.03$. The run was made with bottom plate A and sidewall A, and yielded heat-flux measurements similar to those of Fig. 7. The images in the figure were taken with (a) $\epsilon_0=0.217$,

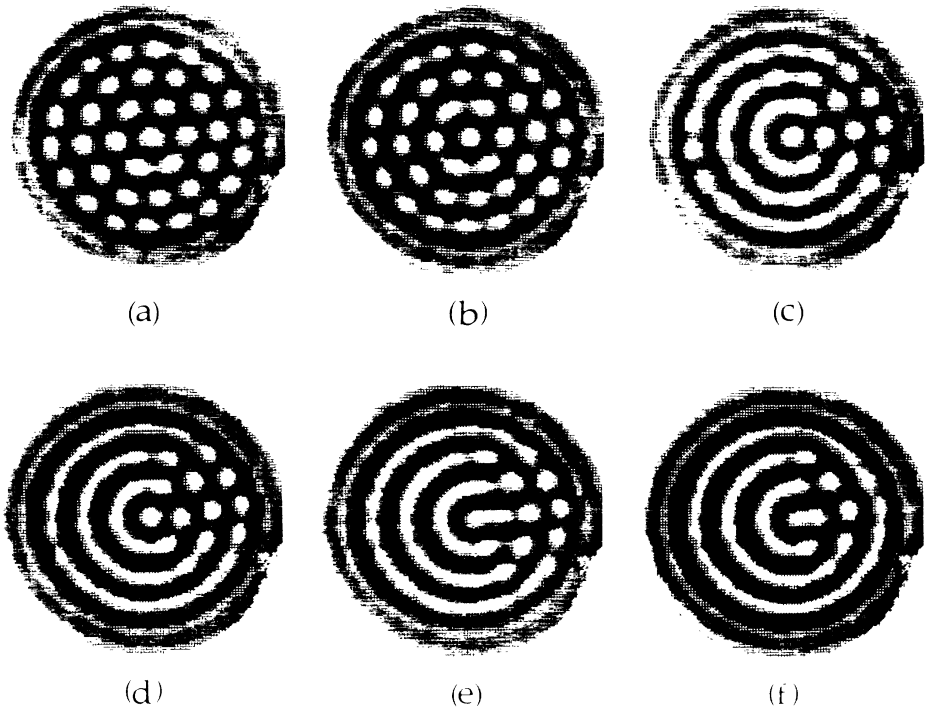

FIG. 10. Shadowgraph images of convective flow patterns for $\omega=15$, $\delta=2.03$, and (a) $\epsilon_0=0.217$, (b) 0.254, (c) 0.289, (d) 0.325, (e) 0.359, and (f) 0.395. Sidewall A was used. The bright regions show downflow at the center of the hexagons, while the dark regions show upflow along their outer boundaries. The images were taken when the patterns were at approximately their peak intensity during the cycle. At these modulation parameters the HS model predicts the boundaries $\epsilon_c=0.142$, $\epsilon_R=0.257$, and $\epsilon_B=0.363$.

(b) 0.254, (c) 0.289, (d) 0.325, (e) 0.359, and (f) 0.395. For the parameters of this run $\epsilon_c=0.142$, $\epsilon_R=0.257$, and $\epsilon_B=0.363$. In Fig. 10(a), where $\epsilon_c<\epsilon_0<\epsilon_R$, the flow observed in the center of the container is clearly cellular, although the pattern adjacent to the sidewall consists of concentric rolls. The cellular flow consists of isolated (or sometimes nearly isolated) regions of downflow (which appear as light areas in the shadowgraph) surrounded on all sides by regions of upflow (dark areas). The cells are aligned in a nearly perfect hexagonal lattice in the center of the container, although the lattice is distorted in the regions closer to the sidewall in order to accommodate the circular geometry of the container. We believe that these cells correspond to the theoretically predicted [33,35] hexagonal cells. The existence of downflow in the cell centers is also as predicted.

The rolls which appear adjacent to the sidewall in Fig. 10(a) probably occur due to two factors: dynamic thermal sidewall forcing, which has been discussed extensively elsewhere [42,46,49–51], and forcing due to fluid flowing underneath the sidewall. The latter effect is due to the expansion or contraction of the fluid in the cell and the sidewalls when the mean temperature is increased or decreased. By the design of sidewall A [see Fig. 6(a)], fluid flows underneath the sidewall to or from the outer channel. Although the flow velocities must be very small, they may contribute significantly to the forcing of parallel rolls in their vicinity.

The circular rolls in the pattern of Fig. 10(a) influence the overall pattern more as ϵ_0 is increased. In 10(b), where $\epsilon_0\approx\epsilon_R$, the cells still exist, but they are slightly connected in the azimuthal direction. In 10(c) the cells have connected to form a circular pattern in most of the cell. In one region of the container, however, the cellular pattern has remained, resulting in an overall pattern which exhibits a coexistence between circular rolls and cells. As ϵ_0 is increased further in Figs. 10(d)–10(f) the coexistence persists, although the region of the container where cells exist decreases in size.

The experimental run described above was repeated several times. Each time the cellular pattern of Fig. 10(a) was reproduced for $\epsilon_c\leq\epsilon_0\leq\epsilon_R$. The orientation of the cells was the same every time. We believe that this reproducible alignment may have been due to thermal perturbations from the thermistor and its leads in bottom plate A, since one of the directions of the constrained lattice is aligned with the groove holding the thermistor (see Fig. 5). The location of the region of coexistence seen in Figs. 10(c)–10(f) was also reproduced.

In Fig. 11 the cellular pattern of Fig. 10(a) is compared to the patterns consisting of irreproducible randomly placed cells that were observed in low-frequency ($\omega=1$) modulation experiments [42–44]. Figure 11(a) shows once again the image of Fig. 10(a), while Fig. 11(b) is from Ref. [44] and shows the emerging pattern from an experimental run with $\omega=1$, $\delta=0.51$, and $\epsilon_0=0.21$. Figures 11(c) and 11(d) are the central portions of the Fourier transforms of Figs. 11(a) and 11(b), respectively (the modulus of the transform is shown as gray levels as a function of the wave-vector components k_x and k_y). The

container used for the run of Fig. 11(b) was also circular, and had as aspect ratio $L=10$. Circular rolls do not exist next to the sidewall in this container because a special sidewall which minimized thermal sidewall forcing [44] was used. The Fourier transform of Fig. 11(a) clearly exhibits sixfold symmetry, while that of Fig. 11(b) does not. The length scales of the patterns also differ. While the average wave number of Fig. 11(a) is $\bar{k}=1.02k_c$, that of Fig. 11(b) is $\bar{k}=1.12k_c$. Finally, the pattern in Fig. 11(a) is reproducible from cycle to cycle, while that of Fig. 11(b) is not. We therefore believe that the cellular flow observed in Fig. 11(a) is not related to the random cellular flow studied in Refs. [42] and [44].

The coexistence observed in Figs. 10(c)–10(f) cannot be reproduced by the HS model, which assumes that the pattern is spatially uniform and on that basis predicts hexagons for Figs. 10(a)–10(d) and rolls for Figs. 10(e) and 10(f). Unfortunately, it is not clear from Fig. 10 whether the coexistence observed would occur in a laterally infinite system, or whether it is due to the forcing of concentric rolls by the sidewall. We therefore made efforts to eliminate this forcing. The two sidewall designs used in Refs. [46] and [44], which were successful in eliminating the forcing for low-frequency modulation and in ramping experiments, were found not to be successful in this case. However, sidewall B (Fig. 6) reduced the forcing sufficiently. With that wall the expanding or contracting fluid generates flow to or from the outer channel through small radial holes located at the midheight of the cell. This flow, since it is not azimuthally symmetric and is symmetric about the midplane, does not force rolls that are parallel to the sidewall. Furthermore, since the spacing of the holes is $0.78d$ and is therefore incommensurate with the wavelength of a roll pattern, the holes should not be able to force rolls that are perpendicular to the wall. Although thermal forcing still exists when using the design of sidewall B, it is apparently not sufficiently strong to dominate the flow pattern if the match between the thermal properties of the fluid and sidewall is adequate. We found that when certain plastics other than acrylic (e.g., Delrin, high-density polyethylene, or chlorinated-polyvinyl chloride, C-PVC) were used with this design, concentric rolls still occurred.

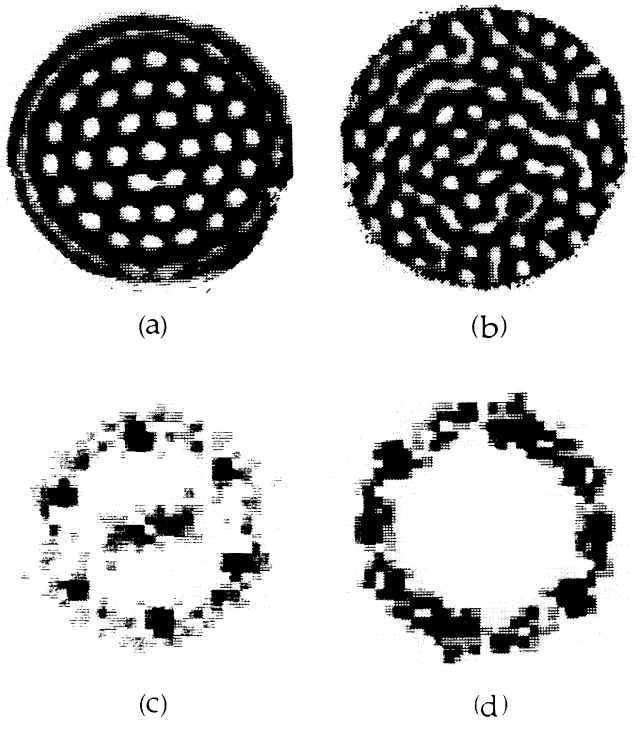

FIG. 11. Comparison of the cellular flow pattern and its Fourier transform observed at $\omega=15$, $\epsilon_0=0.217$, and $\delta=2.03$ with the random cellular flow pattern observed at $\omega=1$, $\epsilon_0=0.21$, and $\delta=0.51$. (a) Figure 10(a), with the low-wave-vector portion of its Fourier transform below it (c), demonstrating the sixfold symmetry of the central portion of the pattern. (b) Image from Ref. [44], which shows the pattern emerging above onset. The low-wave-vector portion of its Fourier transform is below it (d), showing that the intensity of the transform is distributed over a ring instead of having sixfold symmetry.

Figure 12 shows results from an experimental run similar to that of Fig. 10, but with sidewall B and bottom plate A. The heat-flux measurements shown in Fig. 7 were made while obtaining these results. The modulation parameters are $\omega=15$, $\delta=1.97$, and (a) $\epsilon_0=0.214$, (b) 0.253, (c) 0.289, (d) 0.325, (e) 0.363, and (f) 0.398. As before, $\epsilon_c=0.138$, $\epsilon_R=0.252$, and $\epsilon_B=0.356$. In Fig. 12(a) the pattern is once again cellular, and no concentric rolls occur adjacent to the sidewall. The cells, however, do not form a perfect lattice of hexagons. There exists local sixfold symmetry in several regions of the pattern, but these regions are not aligned with each other; this leads to defects in the lattice structure. In Figs. 12(b)–12(e) coexistence is once again observed, but this time the rolls are not all parallel to the sidewall. This result suggests that the coexistence observed in Fig. 10 is perhaps not due to the forcing of rolls by the sidewall, but instead is intrinsic to the problem and would occur in a laterally infinite system. As ϵ_0 is increased through the coexistence range, the ratio of the area of the regions containing hexagons to that of the regions containing rolls decreases. In Fig. 12(f) the pattern is essentially roll-like, although slight signs of cellular flow exist along the perimeter of the pattern. The boundary between the purely cellular region and the coexistence region is consistent with ϵ_R, and the boundary between the coexistence region and the roll region is consistent with ϵ_B. Several other experimental runs were performed with the same sidewall, bottom plate, and modulation parameters. In each run defects appeared in the cellular patterns for $\epsilon_0<0.25$, and in each run the defects were located in different places.

Figure 13 shows a plot of the average wave number as a function of ϵ_0 for $\omega=15$ and $\delta=1.97$. The solid circles correspond to the images shown in Fig. 12. The value of $\bar{k}$ remains nearly constant at $\bar{k}\approx k_c$, varying by only $\approx 1\%$. It is interesting to note that $\bar{k}$ varies with ϵ_0 most smoothly in the regions $0.2\leq\epsilon_0\leq 0.25$ and $0.35\leq\epsilon_0\leq 0.45$, which correspond to the hexagon and roll regions, respectively. In the region between, which corresponds to the coexistence region, the results for $\bar{k}$ are more noisy.

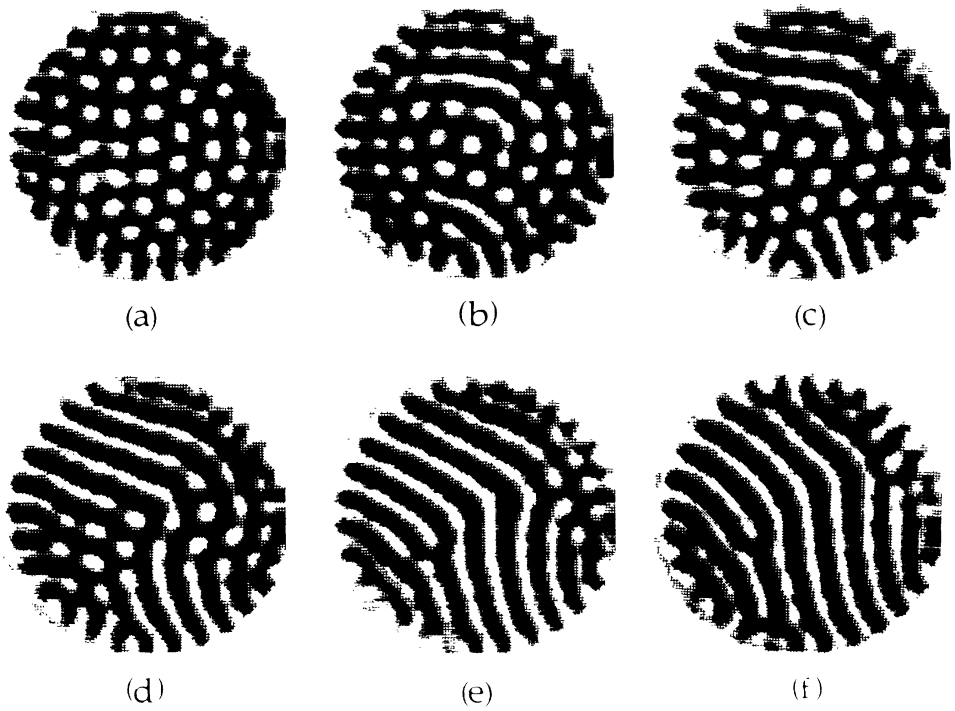

FIG. 12. Images of convective flow patterns as in Fig. 10, but with sidewall B. Modulation parameters are $\omega=15$, $\delta=1.97$, and (a) $\epsilon_0=0.214$, (b) 0.253, (c) 0.289, (d) 0.325, (e) 0.363, (f) 0.398. For these parameters the nine-mode model predicts $\epsilon_c=0.138$, $\epsilon_R=0.252$, and $\epsilon_B=0.356$. Sidewall B was used while obtaining the images shown throughout the remaining part of this paper.

C. The hexagon region

We present in this subsection results obtained within the region $\epsilon_c \leq \epsilon_0 \leq \epsilon_R$. In all examples $\omega=18$ and $\delta=1.99$; for these parameters $\epsilon_c=0.125$ and $\epsilon_R=0.248$. Sidewall B and bottom plate B were used. Bottom plate B was used because of concerns that in bottom plate A the presence of the thermistor directly beneath the cell might cause thermal perturbations in the plate that would influence the pattern; in bottom plate B the thermistor and its leads rest below the sidewall (see Fig. 5).

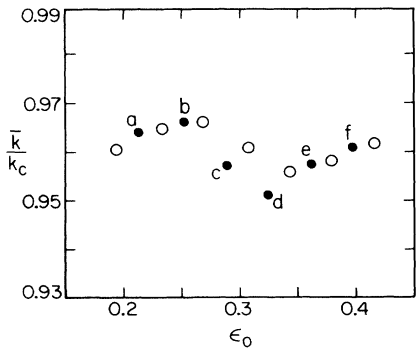

FIG. 13. Average wave number $\bar{k}/k_c$ as a function of ϵ_0 for $\omega=15$ and $\delta=1.97$. The solid circles correspond to the images shown in Fig. 12.

Figure 14 shows the temporal evolution of a roll-like convection pattern after modulation was started. Before the experiment was started, a straight-roll pattern was thermally imprinted by a method similar to that of Chen and Whitehead [52]. It was modulated for 12 cycles with $\epsilon_0=0.382>\epsilon_B$, in order to allow initial transients due to the modulation to end while in the roll region. The pattern during the 12th cycle is shown in Fig. 14(a). After the end of the 12th cycle, ϵ_0 was quenched to 0.191 and the modulation was continued. The evolution is shown in images taken during the (b) 10th, (c) 30th, (d) 50th, and (e) 70th cycle following the quench. In Fig. 14(b) the pattern is essentially unchanged except for a few perturbations near the sidewall. In Fig. 14(c), however, cellular flow is emerging. The pattern in the vicinity of the sidewall is almost completely cellular, while that in the center still has some unbroken segments of the original rolls. In Figs. 14(d) and 14(e) the pattern is almost completely cellular. Cells which are aligned at 60° from the original roll axis can be observed. Despite these signs of sixfold symmetry, the pattern clearly has a number of defects within it.

In order to determine whether such a pattern would eventually evolve to a perfect hexagonal lattice we performed a similar experiment with 256 cycles and with $\epsilon_0=0.183$ after the quench. The results are shown in Fig. 15, where the images were taken during the (a) 136th, (b) 176th, (c) 216th, and (d) 256th cycle. The pattern clearly has not evolved into a perfect lattice, and continues to evolve during the run. It is interesting to note that although $\epsilon_0<\epsilon_R$, coexistence between cells and rolls oc-

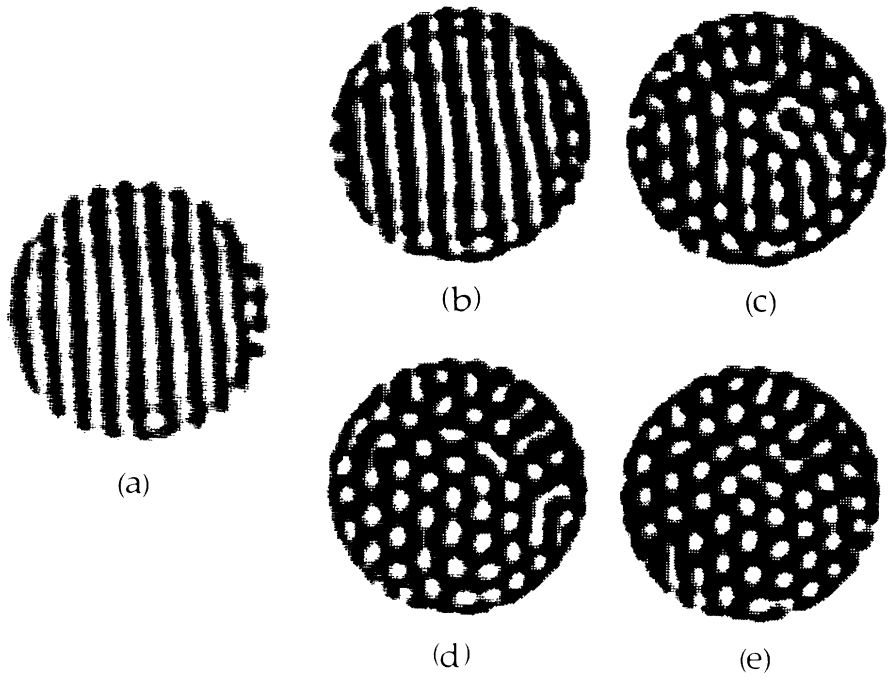

FIG. 14. Evolution of a straight-roll pattern, shown in (a), to a cellular pattern. The modulation parameters are $\omega=18$, $\delta=1.99$, and $\epsilon_0=0.191$. For these parameters $\epsilon_c \leq \epsilon_0 \leq \epsilon_R$. Images (b)–(e) were taken during the (b) 10th, (c) 30th, (d) 50th, and (e) 70th cycle, respectively, after ϵ_0 was quenched from an initial value larger than ϵ_B.

casionally occurs. This is particularly evident in Fig. 15(a), where a long roll segment exists in a pattern that is otherwise almost completely cellular. In Figs. 15(b)–15(d) this roll has disappeared, but several cases where cells have partially connected are observable.

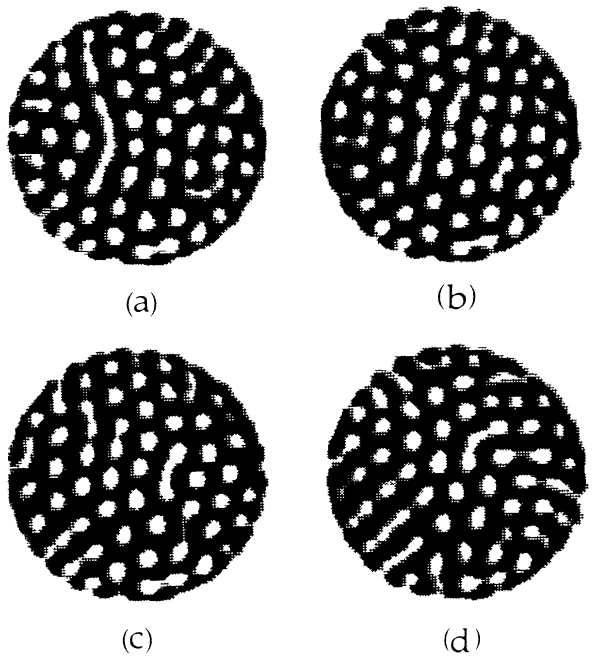

FIG. 15. Long-term evolution of a cellular pattern in the region $\epsilon_c \leq \epsilon_0 \leq \epsilon_R$. The modulation parameters are $\omega=18$, $\delta=1.99$, and $\epsilon_0=0.183$. The images were taken during the (a) 136th, (b) 176th, (c) 216th, and (d) 256th cycle after ϵ_0 was quenched from an initial value larger than ϵ_B.

D. The bistable region

In this subsection we discuss the region $\epsilon_R \leq \epsilon_0 \leq \epsilon_B$. The results shown here were also obtained with bottom plate B and sidewall B. It has already been shown in Fig. 12 that a pattern that is originally cellular evolves to one exhibiting coexistence when ϵ_0 is increased into the bistable region. We also find that a roll-like pattern evolves to one involving coexistence when ϵ_0 is quenched into the bistable region from a value greater than ϵ_B. Such an evolution is shown in Fig. 16, where the modulation parameters are $\omega=15$, $\delta=1.99$, and $\epsilon_0=0.276$. The original pattern was a thermally printed straight-roll pattern. The system was modulated first for 12 cycles at $\epsilon_0=0.387>\epsilon_B$ before quenching into the bistable region. Figure 16(a) was taken during the last cycle before the quench. The other images were taken during the (b) 10th, (c) 50th, (d) 90th, and (e) 130th cycles following the quench. In Fig. 16(b) the pattern has not evolved noticeably except for some minor perturbations around the sidewall. By Fig. 16(c), however, the cellular flow has clearly emerged in certain areas of the cell. These areas tend to be in the vicinity of the sidewall, while in the center of the container much of the original pattern has remained. In Figs. 16(d) and 16(e) the percentage of the pattern that is cellular is roughly the same as in Fig. 16(c), but the pattern has nevertheless evolved, and the regions containing the cells have shifted to different parts of the cell. By Fig. 16(e) the pattern has lost any resemblance to its original form.

In order to determine whether the pattern ever reaches a point where it no longer evolves, we made a run where the system was modulated for over 1000 cycles (this re-

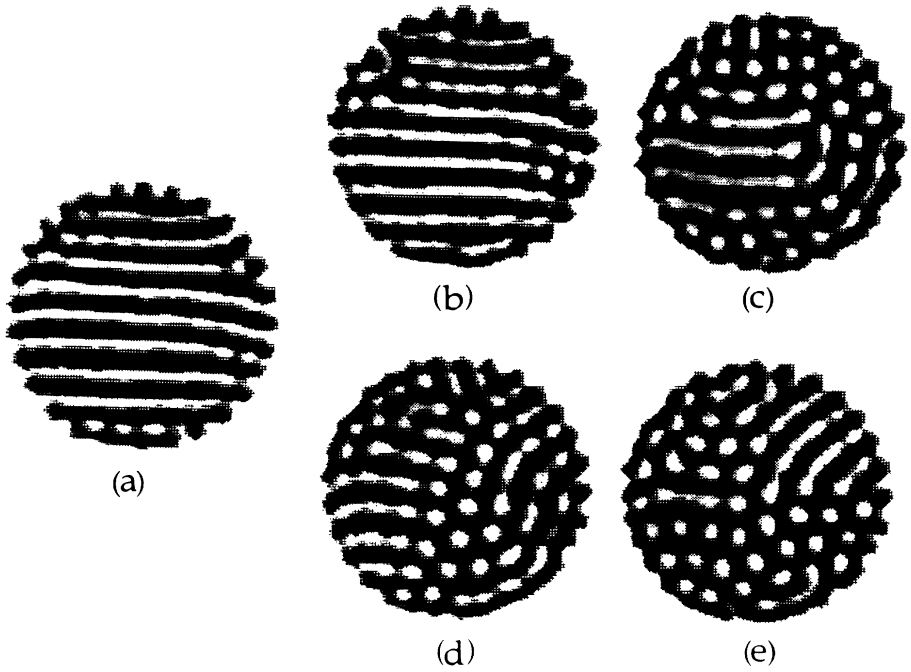

FIG. 16. Evolution of a straight-roll pattern, shown in (a), to one exhibiting coexistence. The modulation parameters are $\omega=15$, $\delta=1.99$, and $\epsilon_0=0.276$. For these parameters $\epsilon_R \leq \epsilon_0 \leq \epsilon_B$. Images (b)–(e) were taken during the (b) 10th, (c) 50th, (d) 90th, and (e) 130th cycle following the quench, respectively.

quired approximately ten hours). The parameters were $\omega=15$, $\delta=1.99$, and $\epsilon_0=0.257$. The modulation was started with a circular roll pattern at $\epsilon_0=0.257$. Images were taken once every 32 cycles. Sample images taken during the (a) 160th, (b) 288th, (c) 416th, (d) 544th, (e) 672nd, and (f) 800th cycle are shown in Fig. 17. During the entire run the pattern remained in a state of evolution. As in Fig. 16, the regions where rolls and cells exist continually change. However, this process is slow, and the patterns in *successive* cycles are very similar to each

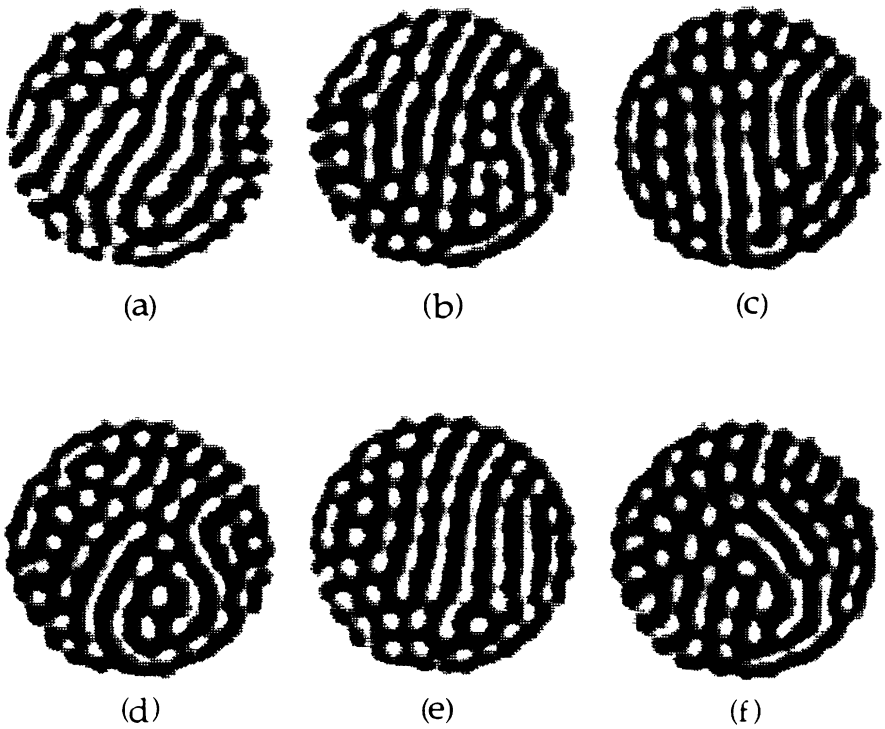

FIG. 17. Long-term evolution of a pattern in the bistable region. The modulation parameters are $\omega=15$, $\delta=1.99$, and $\epsilon_0=0.257$. The images were taken during the (a) 160th, (b) 288th, (c) 416th, (d) 544th, (e) 672nd, and (f) 800th cycle of the modulation.

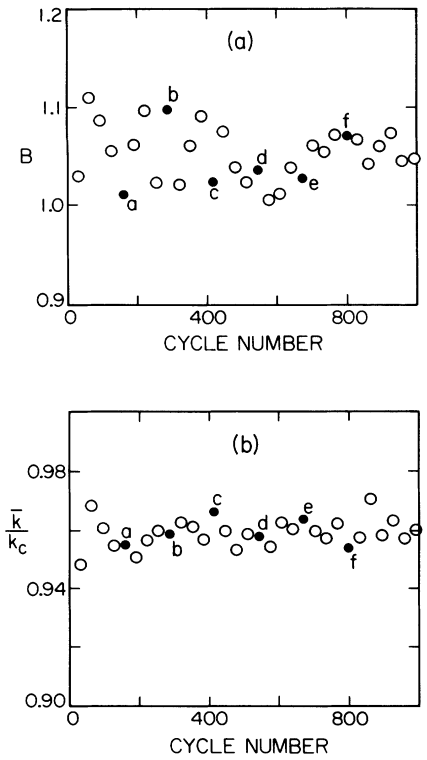

FIG. 18. (a) Boundary length B between the regions of upflow and downflow (see text) as a function of the cycle number for the modulation run of Fig. 17. (b) $\bar{k}/k_c$ as a function of cycle number for the same run. In both plots the solid circles correspond to the images of Fig. 17.

other.

We measured the boundary length B between regions of upflow and downflow [46] (see Sec. III C) in order to quantitatively describe the degree of cellularity of the patterns in the bistable region. We measured B for all the images taken during the experimental run of Fig. 17 in order to observe whether the degree of cellularity would remain constant throughout the run. The results are shown in Fig. 18(a) as a function of the cycle number. The solid circles correspond to the images of Fig. 17. The variations in B are much larger than the experimental resolution, which is illustrated by the smooth variation of B in Refs. [44] and [46]. It is interesting to note that the variation of B from one image to the next is greater during the first half of the run. Nevertheless, it is clear that B is never constant during modulation in the bistable region.

The average wave number of the pattern as a function of the cycle number is shown in Fig. 18(b). The solid circles once again refer to the images in Fig. 17. The values of $\bar{k}/k_c$ do not show any systematic variation throughout the run. The peak-to-peak variations of 2% are consistent with those found between ϵ_R and ϵ_B in Fig. 13, and are larger than the experimental resolution for $\bar{k}$.

In considering the fluctuations in B, shown in Fig. 18(a), it is worth noting that the distinction between cellular and roll-like flow provided by B is quantitative rather than qualitative. We illustrate this in Fig. 19(a) which shows the central portion of a pattern in which rolls and cells coexist in almost the entire cell. For this run the modulation parameters were $\omega=15$, $\delta=1.99$, and $\epsilon_0=0.262$, and the image was taken during the 90th cycle. The image is displayed with one-bit gray scaling in Fig. 19(b), where each pixel whose value is greater than or equal to the mean pixel value is shown as white, and the other pixels are shown as black. Determination of B is made by measuring the boundary length between the black and white regions of the image [46]. With this representation the pattern appears to be almost completely roll-like. The cellular contribution to the pattern can be detected, however, by changing the threshold above which pixels are displayed as white to a higher value, as is done in Fig. 19(c).

E. The roll region

The results for this section were also obtained with bottom plate B and sidewall B.

Theoretical predictions [8,33,35] state that for $\epsilon_0>\epsilon_B$ only rolls are stable, and therefore cellular flow should not be observed. We attempted to experimentally determine this boundary for $\omega=15$ and $\delta=1.99$ ($\epsilon_B=0.356$) in order to compare it with the boundary predicted by

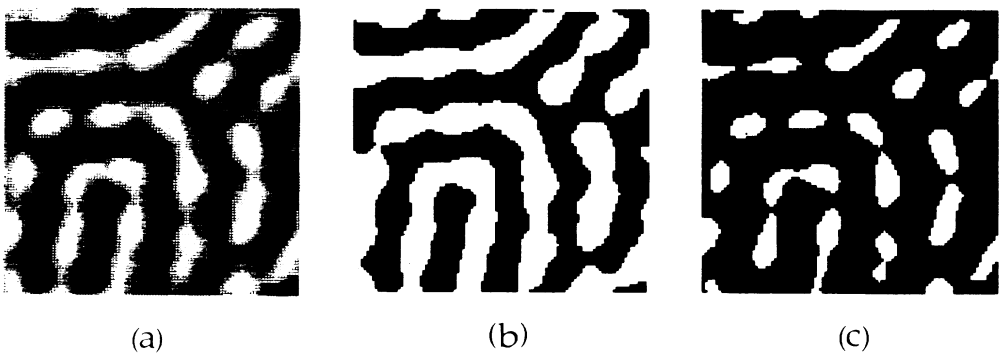

FIG. 19. (a) Central portion of a pattern exhibiting coexistence between roll-like and cellular flow within the same spatial region. (b) The same image as in (a), but displayed with one-bit gray scaling, where pixels with values greater than the mean value are shown as white, and the others as black. (c) One-bit representation of the image in (a), but with an increased threshold value.

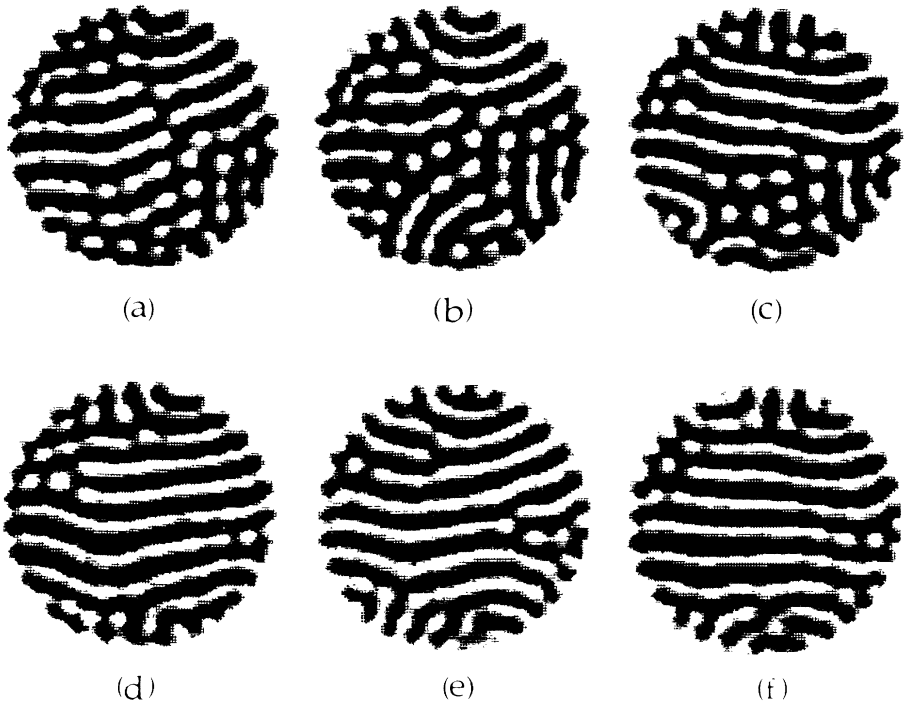

FIG. 20. Evolution of an initial straight-roll pattern after 130 cycles of modulation near ϵ_B. The modulation parameters are $\omega=15$, $\delta=1.99$, and (a) $\epsilon_0=0.327$, (b) 0.335, (c) 0.363, (d) 0.392, (e) 0.446, and (f) 0.471. The value of ϵ_B for these modulation parameters is 0.356.

the HS model. Experimental runs using values of ϵ_0 near ϵ_B were performed in order to determine the value of ϵ_0 above which coexistence would not be observed. For each run we first thermally printed a straight-roll pattern similar to that shown in Fig. 16(a) to use as an initial pattern. We then modulated for 130 cycles to observe whether the initial pattern remained unperturbed. The results are shown in Fig. 20, where all images were taken during the 130th cycle. The values of ϵ_0 were (a) 0.327, (b) 0.335, (c) 0.363, (d) 0.392, (e) 0.446, and (f) 0.471. Cellular flow is seen in all cases. However, in Figs. 20(a)–20(c) cellular flow occurs in the interior regions of the pattern while in Figs. 20(d)–20(f) the cells are found only in the vicinity of the sidewall. Furthermore, in the latter images the original pattern has remained largely undisturbed, while in the first three images many parts of it have gone through considerable evolution. Therefore there is a certain degree of consistency between these results and the predictions of the HS model. Nevertheless, the experimental boundary between the roll region and the coexistence region is not sharp, making it difficult to measure the boundary as a function of ω and δ.

It has been shown in Fig. 17 that for $\epsilon_R \leq \epsilon_0 \leq \epsilon_B$ the pattern, which contains both cellular and roll-like flow, evolves over long time scales. However, even for values of ϵ_0 that are considerably higher than ϵ_B, where cellular flow is generally not seen in the pattern, the pattern continues to evolve over long periods of time. This is shown in Fig. 21, which tracks the evolution of a roll-like pattern for $\omega=15$, $\delta=1.99$, and $\epsilon_0=0.526>\epsilon_B$. For this experiment a horizontal straight-roll pattern was once again thermally printed for use as the initial pattern. The images shown were taken during the (a) 32nd, (b) 160th, (c) 288th, (d) 416th, (e) 544th, and (f) 672nd cycle. In Fig. 21(a) the original pattern is still generally intact. By Fig. 21(b), however, it has evolved significantly. The evolution continues in Figs. 21(c)–21(f). Even at this large ϵ_0, some evidence of coexistence between cellular and roll-like flow is often apparent. In the absence of modulation, such a roll-like pattern would not evolve significantly over the time scale of these experiments.

F. Limitations of the deterministic hexagon-roll stability diagram

The results presented so far have dealt only with values of ω and δ for which cellular and/or roll-like flow relevant to the theoretically predicted [33,35] hexagons could be observed. However, we were not able to observe cellular flow with local sixfold symmetry in all the regions of the parameter space where hexagons are predicted to exist. We present here images of other types of flows that were observed in portions of the theoretically predicted hexagon region. Once again, sidewall B and bottom plate B were used when obtaining these results.

At low modulation amplitudes hexagonal flow did not occur in the hexagon region. Instead, roll-like patterns continued to exist throughout the experimental runs, although the rolls were slightly perturbed. Figure 22 shows images of an initially straight-roll pattern after 130 cycles with $\omega=15$. For Fig. 22(a), $\delta=1.22$ and

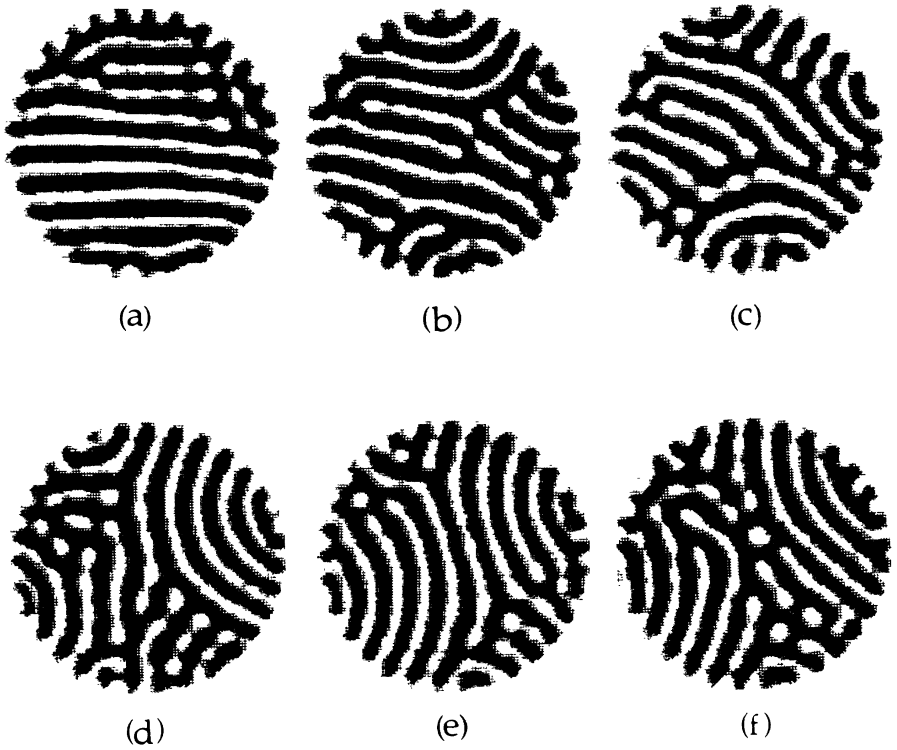

FIG. 21. Evolution of an initial straight-roll pattern during modulation with $\omega=15$, $\delta=1.99$, and $\epsilon_0=0.526>\epsilon_B$. The images were taken during the (a) 32nd, (b) 160th, (c) 288th, (d) 416th, (e) 544th, and (f) 672nd cycle.

$\epsilon_0=0.087$; for Fig. 22(b), $\delta=0.98$ and $\epsilon_0=0.055$. For Fig. 22(a) $\epsilon_c=0.051$, $\epsilon_R=0.095$, and $\epsilon_B=0.163$; for Fig. 22(b) $\epsilon_c=0.032$, $\epsilon_R=0.056$, and $\epsilon_B=0.104$. In Fig. 22(a) the pattern shows mostly cellular flow with local hexagonal symmetry, with a hint of roll formation, as we might expect for ϵ_0 so close to ϵ_R. In Fig. 22(b), however, where ϵ_0 is also very close to ϵ_R, the pattern remains in its original straight-roll form, and only faint signs of modulation of the width of the rolls can be found in certain portions of the pattern. It is possible, of course, that if more cycles were performed in case (b), the roll pattern would eventually evolve to a cellular pattern.

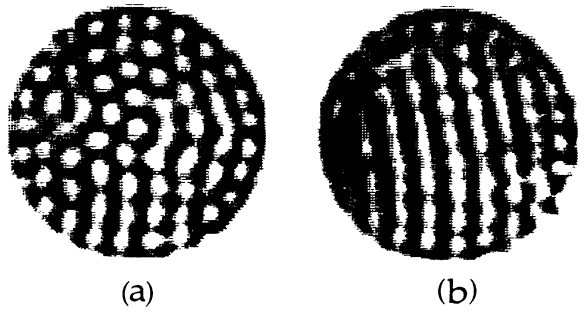

FIG. 22. Evolution of an initial straight-roll pattern during modulation with small δ. The images were taken during the 130th cycle. The modulation parameters are $\omega=15$, with (a) $\delta=1.22$, $\epsilon_0=0.087$, and (b) $\delta=0.98$, $\epsilon_0=0.055$.

At high modulation amplitudes, hexagonal patterns were also not observed. In this case, however, the patterns consisted of randomly positioned cells. For a range of δ, these random cellular patterns were reproducible from one cycle to the next. For δ above this range the patterns were irreproducible from cycle to cycle. Examples are shown in Fig. 23, which is for an experimental run similar to those which yielded Fig. 12, but with $\omega=15$, $\delta=2.85$, and (a) $\epsilon_0=0.377$, (b) 0.404, (c) 0.436, (d) 0.470, (e) 0.496, and (f) 0.529. The heat-flux measurements obtained during this run were shown in Fig. 8(c). The patterns are clearly different from those observed while using smaller values of δ, such as those of Fig. 12. This difference may account for the discrepancy between the experimental and theoretical values of the initial slope S_i of j^{conv}, since the theoretical predictions assume patterns consisting of either an array of rolls or a lattice of hexagons, and the patterns observed clearly consist of neither. Although in this particular run we did not determine the reproducibility of the pattern, other runs with similar modulation parameters yielded similar patterns that were nearly reproducible from one cycle to the next but changed on a longer time scale.

The transition from patterns with local sixfold symmetry to those containing randomly placed cells is shown in Fig. 24, which presents images taken during the 69th cycle of experimental runs with $\omega=15$. The other parameters are (a) $\delta=2.33$, $\epsilon_0=0.266$; (b) $\delta=2.68$, $\epsilon_0=0.350$; (c) $\delta=2.86$, $\epsilon_0=0.350$; and (d) $\delta=3.08$, $\epsilon_0=0.371$. All of these sets of parameters are within the hexagon region.

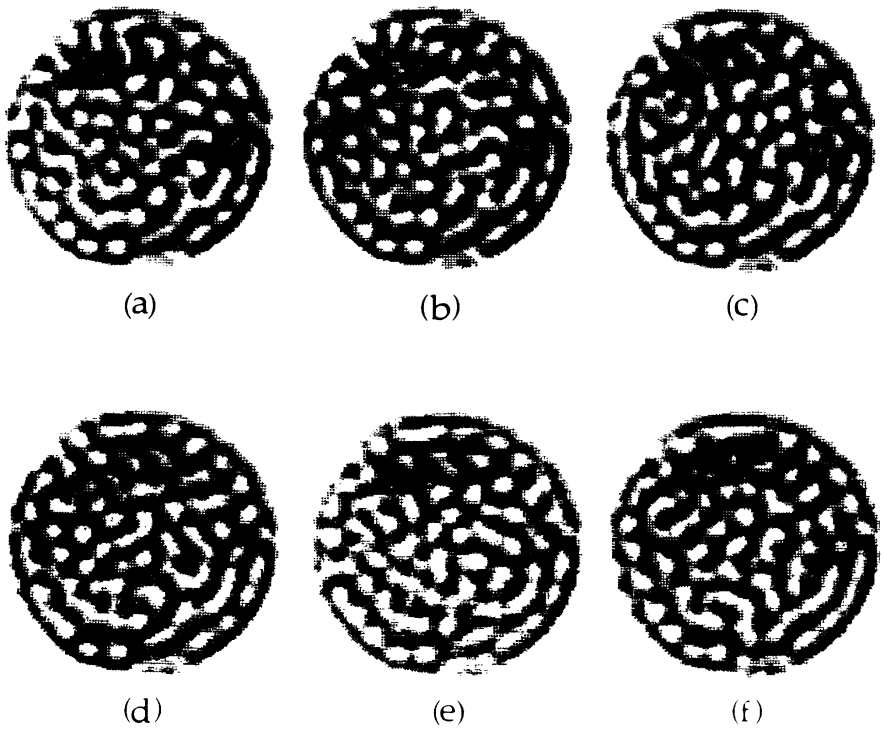

FIG. 23. Flow patterns observed during a run with $\omega=15$, $\delta=2.85$, and increasing values of ϵ_0. The values of ϵ_0 are (a) 0.377, (b) 0.404, (c) 0.436, (d) 0.470, (e) 0.496, and (f) 0.529. The images were taken during the 40th cycle.

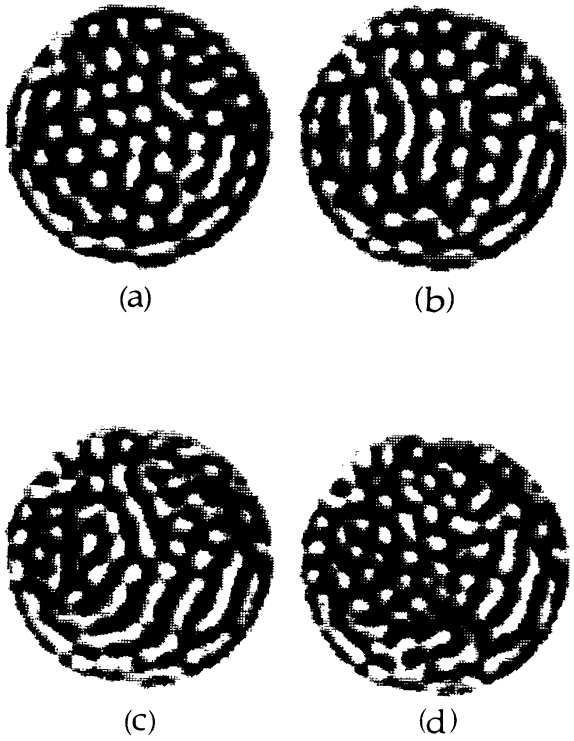

FIG. 24. Flow patterns observed during runs with $\omega=15$ and large values of δ. The images were taken on the 69th cycle. The modulation parameters are (a) $\delta=2.33$, $\epsilon_0=0.266$; (b) $\delta=2.68$, $\epsilon_0=0.350$; (c) $\delta=2.86$, $\epsilon_0=0.350$; and (d) $\delta=3.08$, $\epsilon_0=0.371$.

While the pattern in Fig. 24(a) contains cells with local sixfold symmetry, those of Figs. 24(b)–24(d) show that as δ is increased the patterns progressively exhibit less of this symmetry and are of a more random nature. During the transition between hexagonal flow and random cellular flow, the pattern appears to be composed more of short segments of rolls than of cells, as shown in Figs. 24(b) and 24(c). Images were also taken during the 70th cycle of the runs, and showed that in all four runs the patterns were essentially reproducible from one cycle to the next.

Shown in Fig. 25 are images of patterns taken in the vicinity of the boundary between reproducible and irreproducible flow. The images on top were taken during the 69th cycle, and those on the bottom during the 70th cycle. The modulation frequency is $\omega=13$ (the apparatus was unable to reach this boundary with $\omega=15$), and the other modulation parameters are (a) $\delta=2.82$, $\epsilon_0=0.411$; (b) $\delta=2.99$, $\epsilon_0=0.438$; and (c) $\delta=3.24$, $\epsilon_0=0.429$. All three sets of parameters are located within the hexagon region of the HS model. In Fig. 25(a) most major features of the pattern are reproduced, while in Fig. 25(c) the central portion of the pattern is clearly not reproduced. In Fig. 25(b) a large number of features in this central portion are reproduced, but roughly the same number of features are not. Therefore Fig. 25(b) is roughly at the reproducibility-irreproducibility boundary, which apparently is not very sharp.

Finally, runs were carried out where δ and ϵ_0 were kept constant while ω was varied. The results are shown in

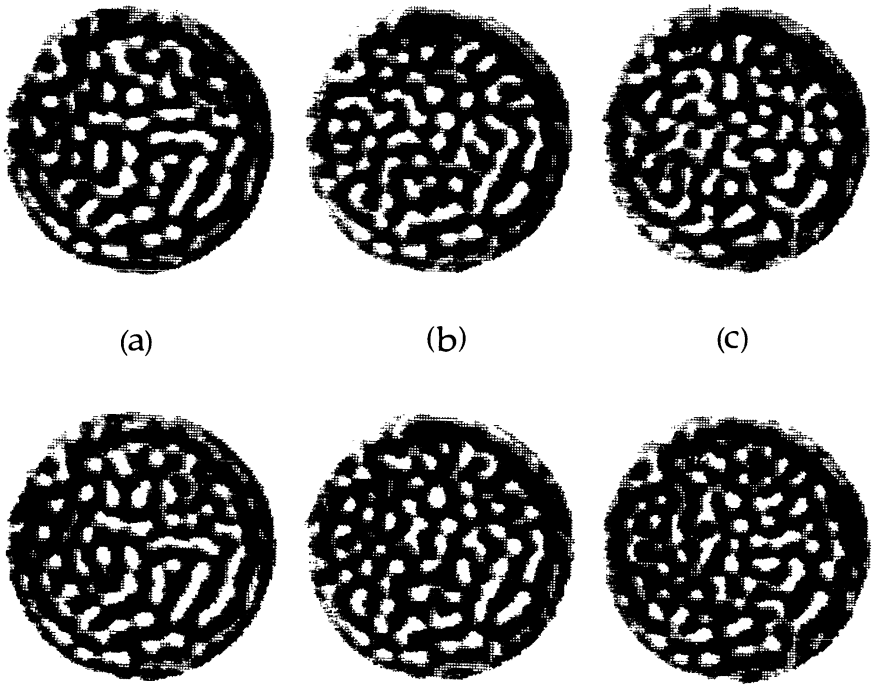

FIG. 25. Patterns observed during experimental runs with $\omega=13.0$, and with the other parameters in the vicinity of the reproducibility/irreproducibility boundary. The images were taken on the (top) 69th and (bottom) 70th cycles. The parameters are (a) $\delta=2.82$, $\epsilon_0=0.411$; (b) $\delta=2.99$, $\epsilon_0=0.438$; and (c) $\delta=3.24$, $\epsilon_0=0.429$. For all cases $\epsilon_c \leq \epsilon_0 \leq \epsilon_R$.

Fig. 26, which presents images from the 69th (left side) and 70th (right side) cycles. The modulation parameters are $\delta \approx 2.0$, $\epsilon_0 \approx 0.22$, and (a) $\omega=8.0$, (b) 9.0, (c) 10.0, and (d) 12.0. In Fig. 26(a) the central portion of the pattern is not reproduced, while in Fig. 26(b) it is partially reproduced. In Figs. 26(c) and 26(d) the entire pattern is essentially reproduced. Note that in Fig. 26(d) signs of local sixfold symmetry occur, while in Fig. 26(c) they do not. Note also the concentric rolls in the vicinity of the sidewall in all patterns of this figure, indicating the increased influence of sidewall forcing at lower modulation frequencies.

We showed in earlier publications [42–44] that in low-frequency modulation experiments ($\omega=1$) there is a threshold convective amplitude below which a pattern cannot sustain itself against stochastic perturbations present in the system. We found that, when ϵ_0 was below a threshold value $\epsilon_S(\delta)$, the pattern consisted of randomly placed cells similar to those shown in Fig. 11(b). The boundary between reproducible roll flow and irreproducible random cellular flow was sharp within experimental resolution [42–44], and semireproducible random cellular flow patterns such as those shown in Figs. 23–26 were not observed. It seems likely to us that during the runs which exhibit semireproducible random cellular flow at the higher frequencies, stochastic perturbations are able to influence the convective patterns slightly without being able to destroy them completely in a given cycle because the amplitude of the convection falls below a threshold value only for a relatively short time.

In the previous low-frequency work it was determined that for $\epsilon_0 < \epsilon_S$ the parameter z of the three-mode Lorenz model [34,45] (which is equivalent to z in the HS model and is proportional to j^{conv}) falls below a threshold $z=10^{-6}$ during part of the cycle, whereas for larger ϵ_0 it always stays above this threshold. It is not clear that z is the best representative of the convective amplitude; the

TABLE I. Minimum values during a cycle of x_{1H}, y_{1H}, and z for the modulation parameters corresponding to the images of Figs. 23–26.

Figure	ω	δ	ϵ_0	$x_{1H}^{\min}$ (units of 10^{-3})	$y_{1H}^{\min}$ (units of 10^{-3})	$z^{\min}$ (units of 10^{-3})
23(a)	15	2.85	0.377	0.99	0.97	99
23(b)	15	2.85	0.404	1.10	1.08	117
23(c)	15	2.85	0.436	1.22	1.19	137
23(d)	15	2.85	0.470	1.35	1.31	154
23(e)	15	2.85	0.496	1.45	1.42	165
23(f)	15	2.85	0.529	1.59	1.55	181
24(a)	15	2.33	0.266	2.50	2.46	160
24(b)	15	2.68	0.350	1.41	1.38	124
24(c)	15	2.86	0.350	0.84	0.82	77
24(d)	15	3.08	0.371	0.45	0.43	40
25(a)	13	2.82	0.411	0.41	0.40	26
25(b)	13	2.99	0.438	0.26	0.25	21
25(c)	13	3.24	0.429	0.08	0.08	6
26(a)	8	1.96	0.213	0.07	0.07	0.13
26(b)	9	1.97	0.229	0.18	0.18	0.82
26(c)	10	1.98	0.210	0.40	0.39	3.16
26(d)	12	1.98	0.220	1.49	1.47	34.2

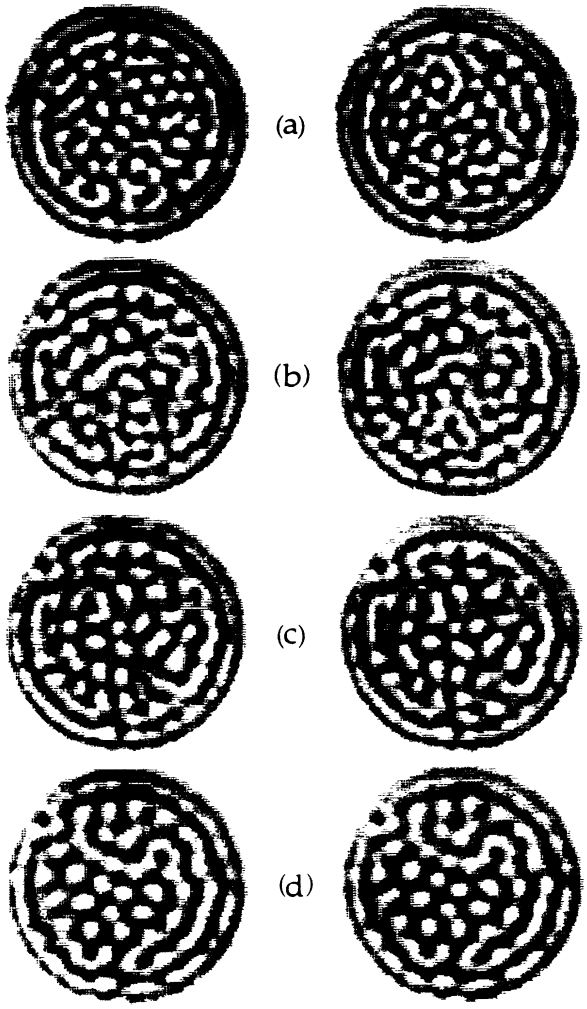

FIG. 26. Patterns observed during runs with $\delta \approx 2.0$ and $\epsilon_0 \approx 0.22$, and whose parameters are in the vicinity of the reproducibility/irreproducibility boundary. The images were taken on the (left) 69th and (right) 70th cycles. The frequencies are (a) $\omega = 8.0$, (b) 9.0, (c) 10.0, and (d) 12.0. For all cases $\epsilon_c \leq \epsilon_0 \leq \epsilon_R$.

amplitude of the lowest Fourier mode of the velocity (x_{1R} or x_{1H} in the HS model) or of the temperature deviation from the conductive profile (y_{1R} or y_{1H}) may be more relevant. Numerical integration of the HS model shows that at low frequencies it does not matter which of these is chosen, because they are strongly coupled by the relations $z \approx x_{1R}^2$, $x_{1R} = y_{1R}$, etc. At low frequencies, therefore, when z falls below 10^{-6}, x_{1R} and y_{1R} fall below 10^{-3}. At the frequencies of the present work this coupling no longer holds. Therefore we have determined the minimum values of x_{1H}, y_{1H}, and z during a modulation cycle for runs with the parameters corresponding to those of Figs. 23–26 and have listed them in Table I. All results are consistent with the hypothesis that fluctuations are able to disturb the convective pattern significantly during a single cycle when x_1 and y_1 fall below a threshold which lies between 1.6×10^{-3} and 2.5×10^{-3}. However, they are not consistent with the hypothesis that the pattern is undisturbed when z remains above 10^{-6}. The values of $x_1^{\min}$ and $y_1^{\min}$ at the pattern reproducibility-irreproducibility boundary vary somewhat with ω. Therefore a more sophisticated theoretical approach must be used for the detailed prediction of this boundary. It would be interesting to examine the Langevin model used by Swift and Hohenberg [53] at our present frequencies to determine mean attractor lifetimes.

V. CONCLUSION

In this paper we have presented heat-flux measurements and shadowgraph images which revealed competition between cellular and roll-like patterns in convective flows in a thin horizontal fluid layer subjected to a temperature difference which is modulated at moderately high amplitudes and frequencies. Over the theoretically predicted range $\epsilon_c \leq \epsilon_0 \leq \epsilon_R$, we observed cellular flow with local sixfold symmetry. For $\epsilon_R \leq \epsilon_0 \leq \epsilon_B$, a pattern exhibiting coexistence between cellular and roll-like flow was observed. For $\epsilon_0 > \epsilon_B$, rolls were observed. All patterns were essentially reproducible from one modulation cycle to the next, but evolved on much longer time scales than a modulation period. At high modulation amplitudes, the patterns consisted of randomly located cells at all values of ϵ_0 studied. These cells also were essentially reproducible from one cycle to the next and evolved on long time scales. At still higher modulation amplitudes, the random cellular patterns became irreproducible from one cycle to the next and were similar to those observed previously [42,44,46] at much smaller modulation frequencies and in temporal ramps through the threshold.

Some of the results were in good agreement with theory and others were unexpected. Among those in agreement with theory were the measurements of the convective threshold shift and the observation at moderately large modulation amplitudes of cellular patterns with local sixfold symmetry over the range where hexagons were theoretically predicted to be stable. It is not surprising that perfect hexagonal patterns were not observed in these experiments when one considers that under steady heating in finite containers the roll patterns that are observed are frequently not straight and parallel as theoretically predicted for an infinite system, but instead are bent and contain defects such as grain boundaries and dislocations.

The results which are not explained by the model are likely to be associated with the fact that over a wide parameter range the pattern amplitude periodically decays to microscopic levels during part of each cycle. When the amplitude is sufficiently small, the pattern can be altered by stochastic effects associated either with thermal noise or with external noise inherent in the experiment. An important result which differed from the model prediction was the observation of coexistence of cellular and roll-like flow over the range $\epsilon_R \leq \epsilon_0 \leq \epsilon_B$. The coexistence explains the absence of the theoretically predicted hysteresis loop in the heat-flux measurements over this range. Coexistence was not predicted because the theoretical models [33,35] *assumed* a spatially homogene-

ous pattern. Further theoretical work is therefore required in order to understand this phenomenon. Presumably a model with spatial variation and possible stochastic forces would result in a pattern which is a mixture of rolls and hexagons, in proportions which vary smoothly from pure hexagons to pure rolls as ϵ_0 varies from ϵ_R to ϵ_B.

The observation at *high* modulation amplitudes of patterns involving randomly placed cells and short roll segments was also unpredicted. We believe that these patterns may be due to the influence of stochastic perturbations which become important during the part of the modulation cycle when the amplitude becomes very small.

A comparison between experimental results on modulated convection and classical non-OB convection is instructive. The possibility of stochastic perturbations in modulated convection is a factor which is absent in the usual non-OB case associated with temperature-dependent fluid properties, because there the amplitudes never are small and stochastic forces are negligible. Indeed, the coexistence of cells and rolls over the entire range from ϵ_R to ϵ_B, which is shown in Figs. 10 and 12, does not occur. Instead, hexagons (rolls) give way to rolls (hexagons) at a nearly unique value $\epsilon_{T'}$ of ϵ_0 as ϵ_0 is increased (decreased) [20]. The value of $\epsilon_{T'}$ can be identified as the value of ϵ_0 at which the generalized potentials for the two phases (hexagons and rolls) become equal. Equilibration between the two phases in this case occurs via nucleation near the cell walls, and stochastic effects do not appear to play a significant role. In the modulated case there is no potential, even near threshold. It is difficult to know which, if any, of the observed effects are associated with the corresponding lack of an extremum principle.

ACKNOWLEDGMENTS

We are grateful to J. B. Swift and P. C. Hohenberg for valuable discussions. This work was supported by U.S. Department of Energy Grant No. DE-FG03-87ER13738.

[1] S. Chandrasekhar, *Hydrodynamic and Hydromagnetic Stability* (Oxford University Press, London, 1961).

[2] H. Bénard, Rev. Gen. Sci. Pures Appl. **11**, 1261 (1900); **11**, 1309 (1900); Ann. Chim. Phys. **23**, 62 (1901).

[3] A large literature pertaining to this field has evolved. Particularly useful as introductions to early work are the reviews by E. L. Koschmieder, Adv. Chem. Phys. **26**, 177 (1974); in *Order and Fluctuations in Equilibrium and Nonequilibrium Statistical Mechanics,* XVIIth International Solvay Conference, edited by G. Nicolis, G. Dewal, and J. W. Turner (Wiley, New York, 1981), p. 168; F. Busse, in *Hydrodynamic Instabilities and the Transition to Turbulence,* edited by H. L. Swinney and J. P. Gollub (Springer, Berlin, 1985), p. 97; Rep. Prog. Phys. **41**, 1929 (1978).

[4] A. Oberbeck, Ann. Phys. Chem. **7**, 271 (1879).

[5] J. Boussinesq, *Théorie Analytique de la Chaleur* (Gauthier-Villars, Paris, 1903), Vol. 2.

[6] A. Schlüter, D. Lortz, and F. Busse, J. Fluid Mech. **23**, 129 (1965).

[7] See, for instance, F. Busse, in *Hydrodynamic Instabilities and the Transition to Turbulence,* edited by H. L. Swinney and J. P. Gollub (Springer, Berlin, 1981).

[8] F. Busse, J. Fluid Mech. **30**, 625 (1967).

[9] E. Palm, J. Fluid Mech. **8**, 183 (1960).

[10] L. A. Segel and J. T. Stuart, J. Fluid Mech. **13**, 289 (1962).

[11] E. Palm, T. Ellingsen, and B. Gjerik, J. Fluid Mech. **30**, 651 (1967).

[12] S. H. Davis and L. A. Segel, Phys. Fluids **11**, 478 (1968).

[13] F. H. Busse, in *Mantle Convection, Plate Tectonics, and Global Dynamics,* edited by W. R. Peltier, Vol. 4 of *The Fluid Mechanics of Astrophysics and Geophysics* (Gordon and Breach, New York, 1989).

[14] C. Q. Hoard, C. R. Robertson, and A. Acrivos, Int. J. Heat Mass Transfer **13**, 849 (1970).

[15] M. Dubois, P. Bergé, and J. Wesfried, J. Phys. **39**, 1253 (1978).

[16] R. W. Walden and G. Ahlers, J. Fluid Mech. **109**, 89 (1981).

[17] S. Ciliberto, E. Pampaloni, and C. Perez-Garcia, Phys. Rev. Lett. **61**, 1198 (1988).

[18] S. Ciliberto, P. Coullet, J. Lega, E. Pampaloni, and C. Perez-Garcia, Phys. Rev. Lett. **65**, 2370 (1990).

[19] E. Bodenschatz, J. de Bruyn, G. Ahlers, and D. S. Cannell, Bull. Am. Phys. Soc. **36**, 653 (1991).

[20] E. Bodenschatz, J. de Bruyn, G. Ahlers, and D. S. Cannell, Phys. Rev. Lett. **67**, 3078 (1991).

[21] P. H. Roberts, J. Fluid Mech. **30**, 33 (1967).

[22] M. Tveitereid and E. Palm, J. Fluid Mech. **76**, 481 (1976).

[23] M. Tveitereid, Int. J. Heat Mass Transfer **21**, 335 (1978).

[24] D. J. Tritton and M. N. Zarraga, J. Fluid Mech. **30**, 21 (1967).

[25] R. Krishnamurti, J. Fluid Mech. **33**, 445 (1968); **33**, 457 (1968).

[26] J. B. Swift and P. C. Hohenberg, Phys. Rev. A **39**, 4132 (1989).

[27] As noted by Busse (in Ref. [13]) and discussed by Swift and Hohenberg (Ref. [26]), Ref. [25] contained a sign error which yielded the incorrect flow direction for the hexagons.

[28] S. Rosenblat and D. M. Herbert, J. Fluid. Mech. **43**, 385 (1969).

[29] S. Rosenblat and G. A. Tanaka, Phys. Fluids **14**, 1319 (1971).

[30] For a comprehensive review of early work, see S. H. Davis, Annu. Rev. Fluid Mech. **8**, 57 (1976).

[31] R. G. Finucane and R. E. Kelly, Int. J. Heat Mass Transfer **19**, 71 (1976).

[32] G. Ahlers, P. C. Hohenberg, and M. Lücke, Phys. Rev. Lett. **53**, 48 (1984).

[33] M. N. Roppo, S. H. Davis, and S. Rosenblat, Phys. Fluids **27**, 796 (1984).

[34] G. Ahlers, P. C. Hohenberg, and M. Lücke, Phys. Rev. A **32**, 3493 (1985).

[35] P. C. Hohenberg and J. B. Swift, Phys Rev. A **35**, 3855 (1987).

[36] J. B. Swift and P. C. Hohenberg, Phys. Rev. A **36**, 4870 (1987).
[37] J. P. Gollub and S. V. Benson, Phys. Rev. Lett. **41**, 948 (1978).
[38] G. Ahlers, P. C. Hohenberg, and M. Lücke, Phys. Rev. A **32**, 3519 (1985).
[39] J. J. Niemela and R. J. Donnelly, Phys. Rev. Lett. **57**, 583 (1986).
[40] J. J. Niemela and R. J. Donnelly, Phys. Rev. Lett. **59**, 2431 (1987).
[41] C. W. Meyer, G. Ahlers, and D. S. Cannell, Bull. Am. Phys. Soc. **32**, 2040 (1987).
[42] C. W. Meyer, G. Ahlers, and D. S. Cannell, Phys. Rev. Lett. **59**, 1577 (1987).
[43] G. Ahlers, C. W. Meyer, and D. S. Cannell, J. Stat. Phys. **54**, 1121 (1989).
[44] C. W. Meyer, G. Ahlers, and D. S. Cannell (unpublished).
[45] E. N. Lorenz, J. Atmos. Sci. **20**, 130 (1963).
[46] C. W. Meyer, G. Ahlers, and D. S. Cannell, Phys. Rev. A **44**, 2514 (1991).
[47] C. W. Meyer, G. Ahlers, and D. S. Cannell, Bull. Am. Phys. Soc. **33**, 370 (1988).
[48] C. W. Meyer, D. S. Cannell, G. Ahlers, J. B. Swift, and P. C. Hohenberg, Phys. Rev. Lett. **61**, 947 (1988).
[49] G. Ahlers, M. C. Cross, P. C. Hohenberg, and S. Safran, J. Fluid Mech. **110**, 297 (1981).
[50] M. C. Cross, P. C. Hohenberg, and M. C. Lücke, J. Fluid Mech. **136**, 169 (1983).
[51] V. Steinberg, G. Ahlers, and D. S. Cannell, Phys. Scr. **32**, 534 (1985).
[52] M. M. Chen and J. A. Whitehead, J. Fluid Mech. **31**, 1 (1968).
[53] J. B. Swift and P. C. Hohenberg, Phys. Rev. Lett. **60**, 75 (1988).

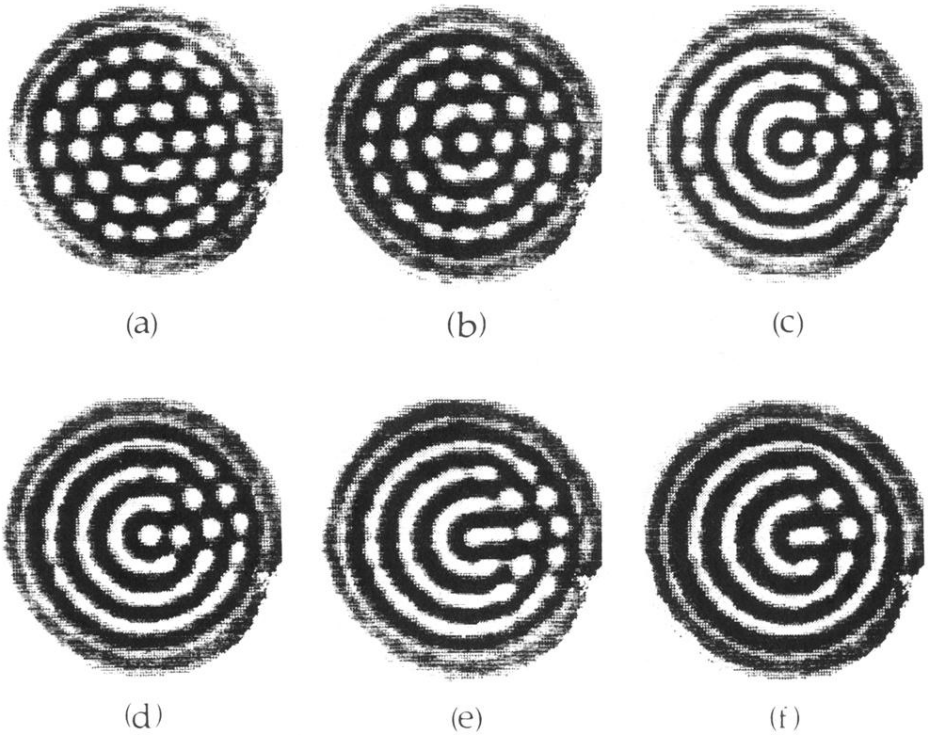

FIG. 10. Shadowgraph images of convective flow patterns for $\omega=15$, $\delta=2.03$, and (a) $\epsilon_0=0.217$, (b) 0.254, (c) 0.289, (d) 0.325, (e) 0.359, and (f) 0.395. Sidewall A was used. The bright regions show downflow at the center of the hexagons, while the dark regions show upflow along their outer boundaries. The images were taken when the patterns were at approximately their peak intensity during the cycle. At these modulation parameters the HS model predicts the boundaries $\epsilon_c=0.142$, $\epsilon_R=0.257$, and $\epsilon_B=0.363$.

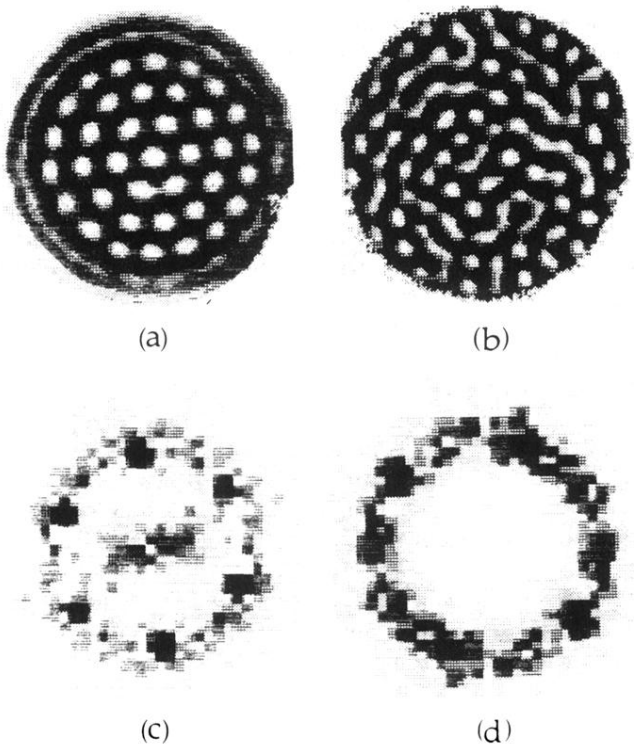

FIG. 11. Comparison of the cellular flow pattern and its Fourier transform observed at $\omega=15$, $\epsilon_0=0.217$, and $\delta=2.03$ with the random cellular flow pattern observed at $\omega=1$, $\epsilon_0=0.21$, and $\delta=0.51$. (a) Figure 10(a), with the low-wave-vector portion of its Fourier transform below it (c), demonstrating the sixfold symmetry of the central portion of the pattern. (b) Image from Ref. [44], which shows the pattern emerging above onset. The low-wave-vector portion of its Fourier transform is below it (d), showing that the intensity of the transform is distributed over a ring instead of having sixfold symmetry.

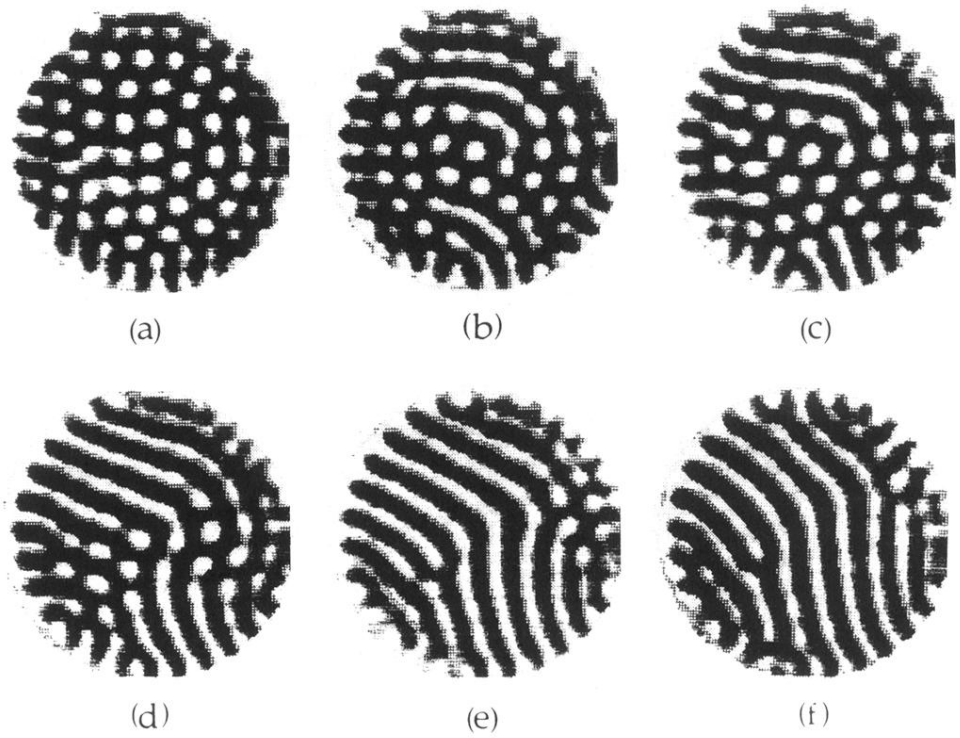

FIG. 12. Images of convective flow patterns as in Fig. 10, but with sidewall B. Modulation parameters are $\omega=15$, $\delta=1.97$, and (a) $\epsilon_0=0.214$, (b) 0.253, (c) 0.289, (d) 0.325, (e) 0.363, (f) 0.398. For these parameters the nine-mode model predicts $\epsilon_c=0.138$, $\epsilon_R=0.252$, and $\epsilon_B=0.356$. Sidewall B was used while obtaining the images shown throughout the remaining part of this paper.

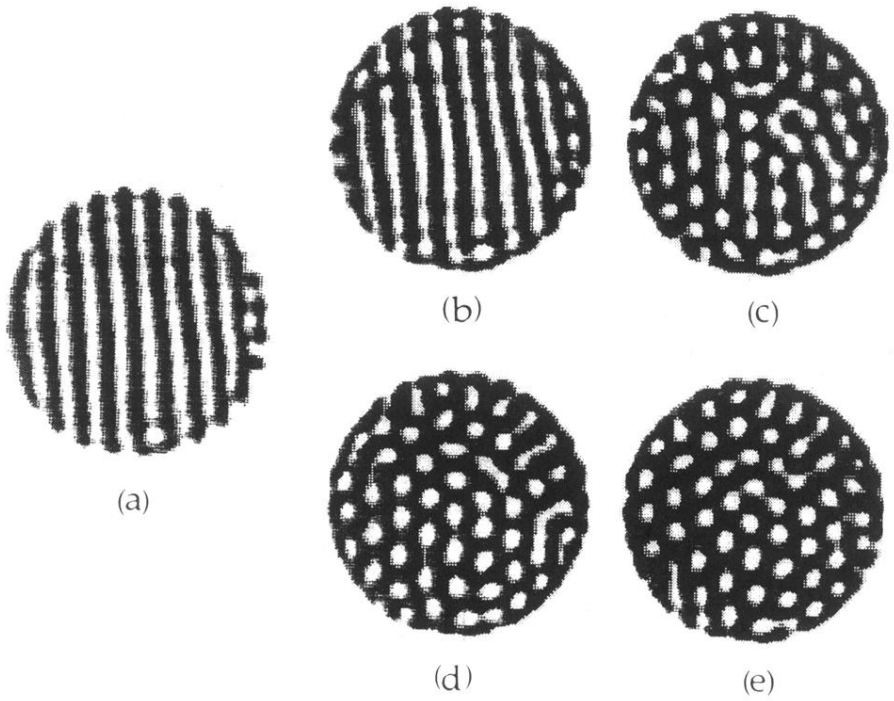

FIG. 14. Evolution of a straight-roll pattern, shown in (a), to a cellular pattern. The modulation parameters are $\omega=18$, $\delta=1.99$, and $\epsilon_0=0.191$. For these parameters $\epsilon_c \leq \epsilon_0 \leq \epsilon_B$. Images (b)–(e) were taken during the (b) 10th, (c) 30th, (d) 50th, and (e) 70th cycle, respectively, after ϵ_0 was quenched from an initial value larger than ϵ_B.

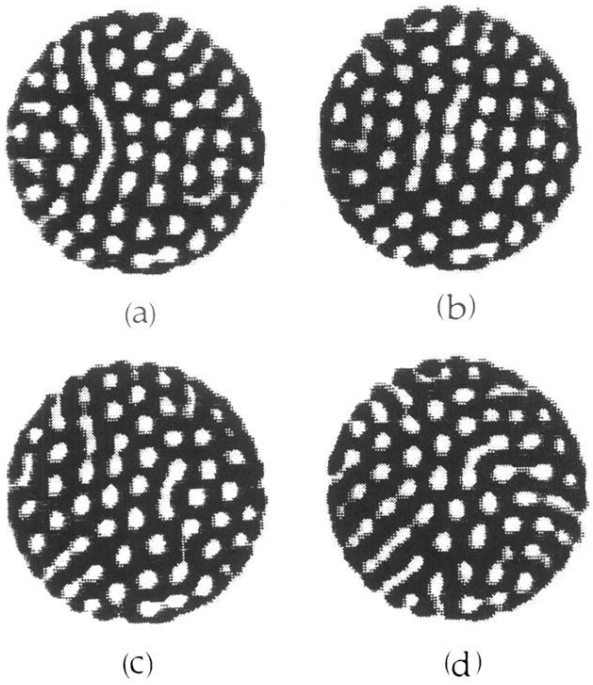

FIG. 15. Long-term evolution of a cellular pattern in the region $\epsilon_c \leq \epsilon_0 \leq \epsilon_R$. The modulation parameters are $\omega = 18$, $\delta = 1.99$, and $\epsilon_0 = 0.183$. The images were taken during the (a) 136th, (b) 176th, (c) 216th, and (d) 256th cycle after ϵ_0 was quenched from an initial value larger than ϵ_B.

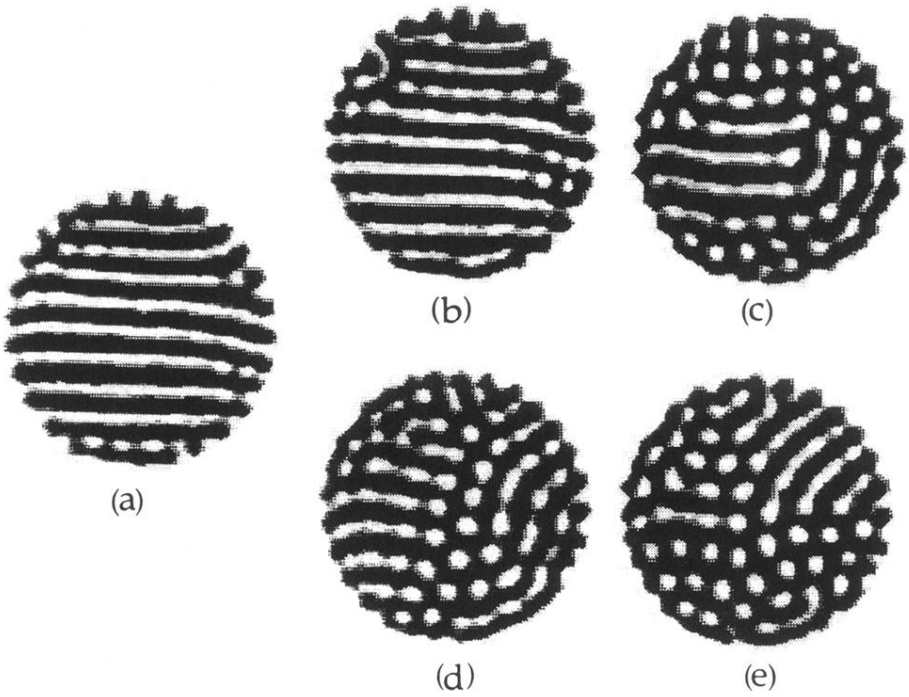

FIG. 16. Evolution of a straight-roll pattern, shown in (a), to one exhibiting coexistence. The modulation parameters are $\omega=15$, $\delta=1.99$, and $\epsilon_0=0.276$. For these parameters $\epsilon_R \leq \epsilon_0 \leq \epsilon_B$. Images (b)–(e) were taken during the (b) 10th, (c) 50th, (d) 90th, and (e) 130th cycle following the quench, respectively.

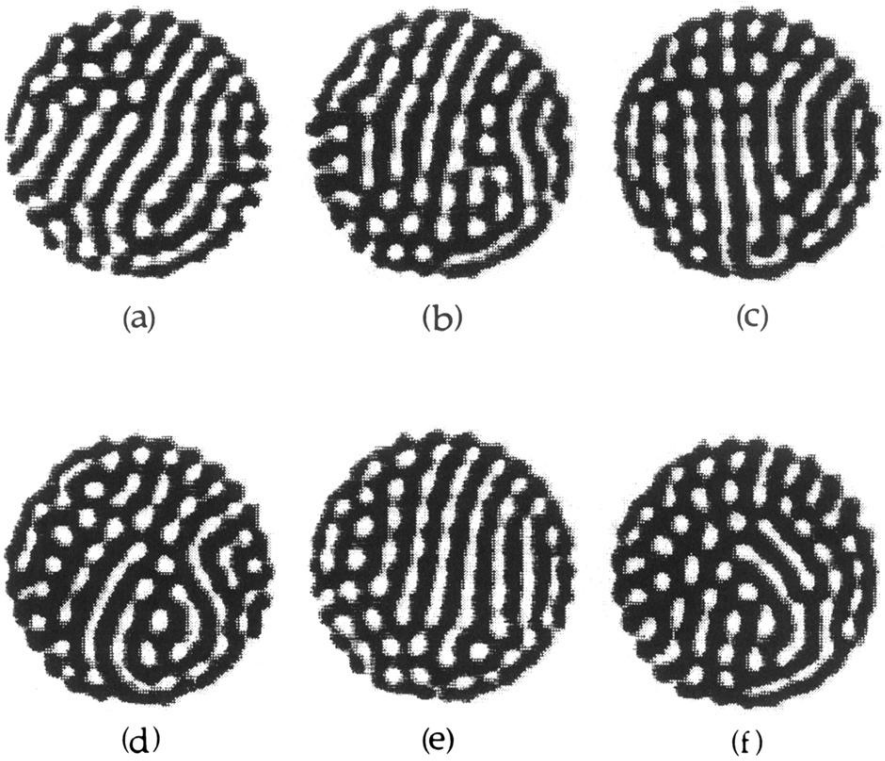

FIG. 17. Long-term evolution of a pattern in the bistable region. The modulation parameters are $\omega=15$, $\delta=1.99$, and $\epsilon_0=0.257$. The images were taken during the (a) 160th, (b) 288th, (c) 416th, (d) 544th, (e) 672nd, and (f) 800th cycle of the modulation.

FIG. 19. (a) Central portion of a pattern exhibiting coexistence between roll-like and cellular flow within the same spatial region. (b) The same image as in (a), but displayed with one-bit gray scaling, where pixels with values greater than the mean value are shown as white, and the others as black. (c) One-bit representation of the image in (a), but with an increased threshold value.

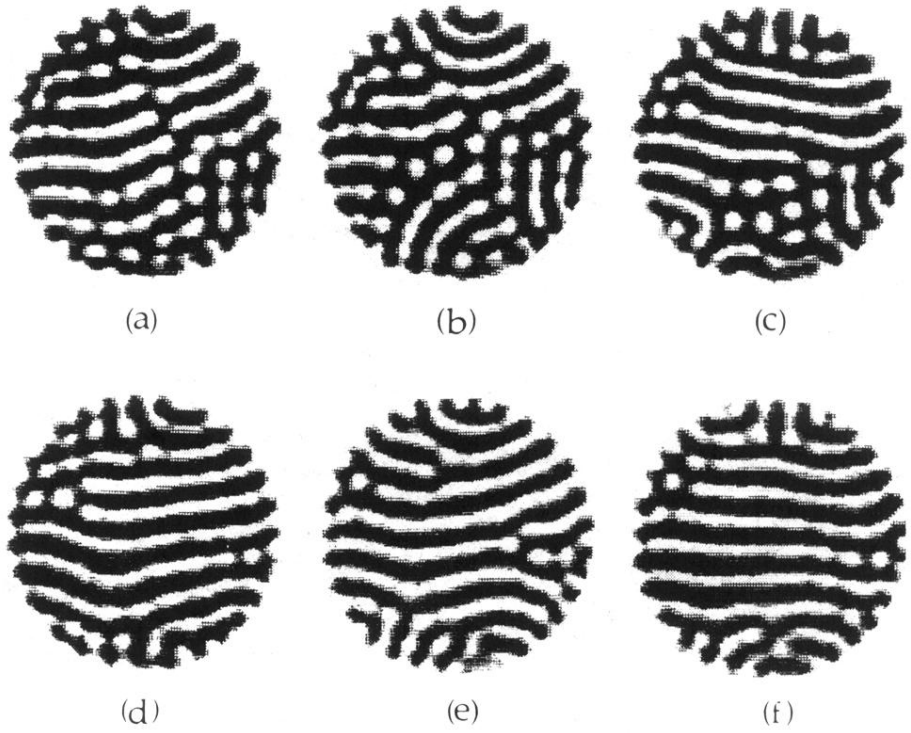

FIG. 20. Evolution of an initial straight-roll pattern after 130 cycles of modulation near ϵ_B. The modulation parameters are $\omega=15$, $\delta=1.99$, and (a) $\epsilon_0=0.327$, (b) 0.335, (c) 0.363, (d) 0.392, (e) 0.446, and (f) 0.471. The value of ϵ_B for these modulation parameters is 0.356.

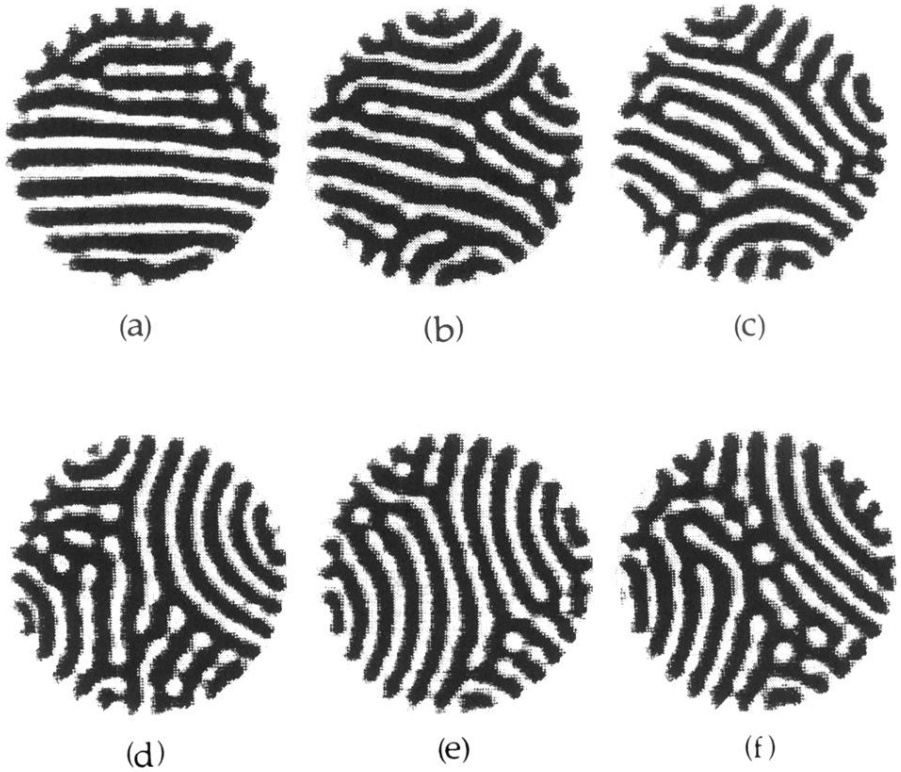

FIG. 21. Evolution of an initial straight-roll pattern during modulation with $\omega=15$, $\delta=1.99$, and $\epsilon_0=0.526>\epsilon_B$. The images were taken during the (a) 32nd, (b) 160th, (c) 288th, (d) 416th, (e) 544th, and (f) 672nd cycle.

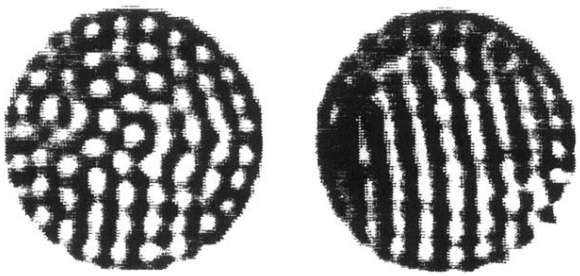

FIG. 22. Evolution of an initial straight-roll pattern during modulation with small δ. The images were taken during the 130th cycle. The modulation parameters are $\omega=15$, with (a) $\delta=1.22$, $\epsilon_0=0.087$, and (b) $\delta=0.98$, $\epsilon_0=0.055$.

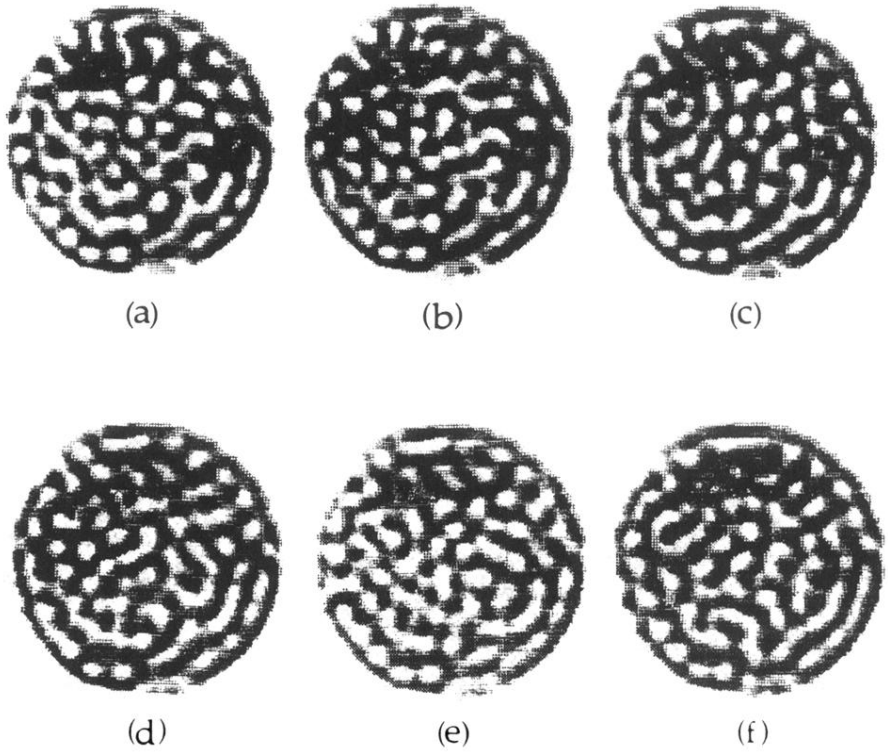

FIG. 23. Flow patterns observed during a run with $\omega=15$, $\delta=2.85$, and increasing values of ϵ_0. The values of ϵ_0 are (a) 0.377, (b) 0.404, (c) 0.436, (d) 0.470, (e) 0.496, and (f) 0.529. The images were taken during the 40th cycle.

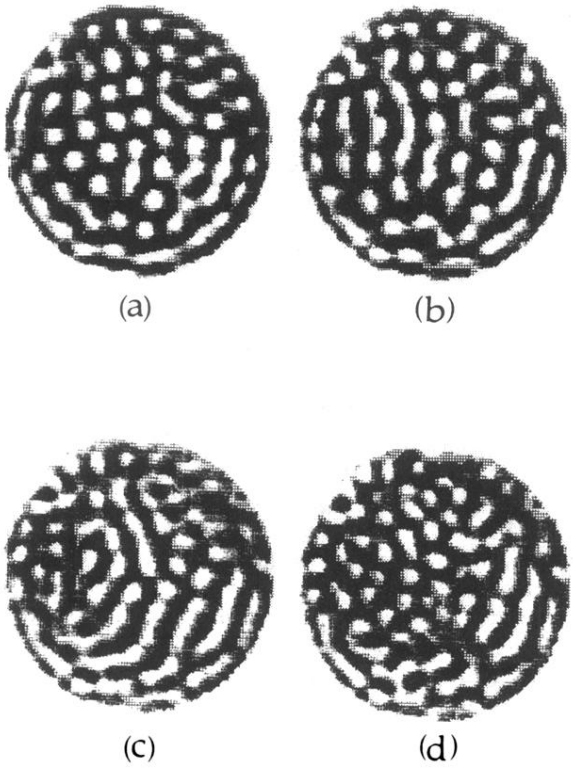

FIG. 24. Flow patterns observed during runs with $\omega = 15$ and large values of δ. The images were taken on the 69th cycle. The modulation parameters are (a) $\delta = 2.33$, $\epsilon_0 = 0.266$; (b) $\delta = 2.68$, $\epsilon_0 = 0.350$; (c) $\delta = 2.86$, $\epsilon_0 = 0.350$; and (d) $\delta = 3.08$, $\epsilon_0 = 0.371$.

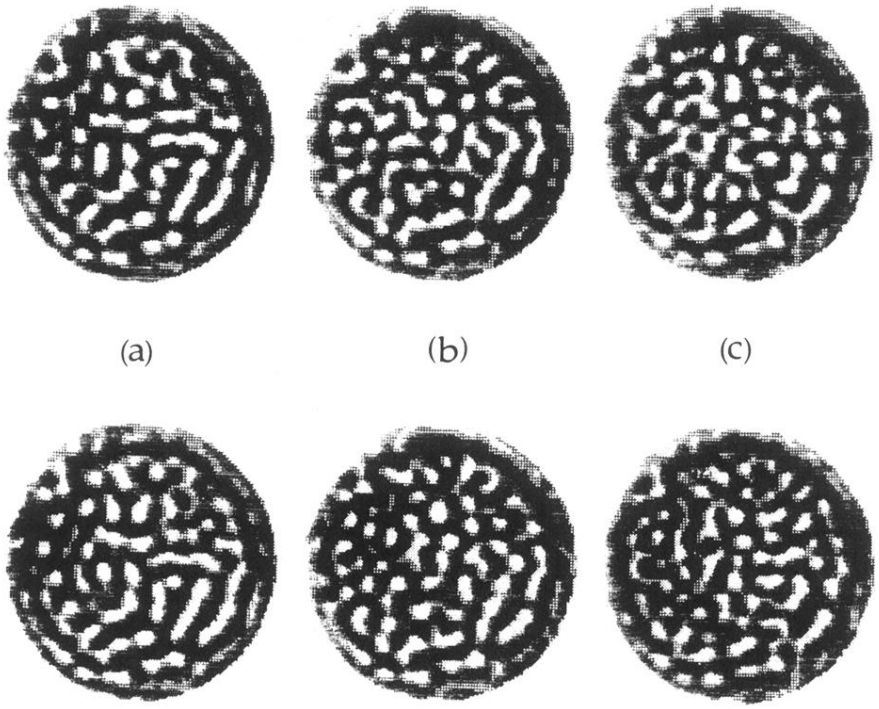

FIG. 25. Patterns observed during experimental runs with $\omega = 13.0$, and with the other parameters in the vicinity of the reproducibility/irreproducibility boundary. The images were taken on the (top) 69th and (bottom) 70th cycles. The parameters are (a) $\delta = 2.82$, $\epsilon_0 = 0.411$; (b) $\delta = 2.99$, $\epsilon_0 = 0.438$; and (c) $\delta = 3.24$, $\epsilon_0 = 0.429$. For all cases $\epsilon_c \leq \epsilon_0 \leq \epsilon_R$.

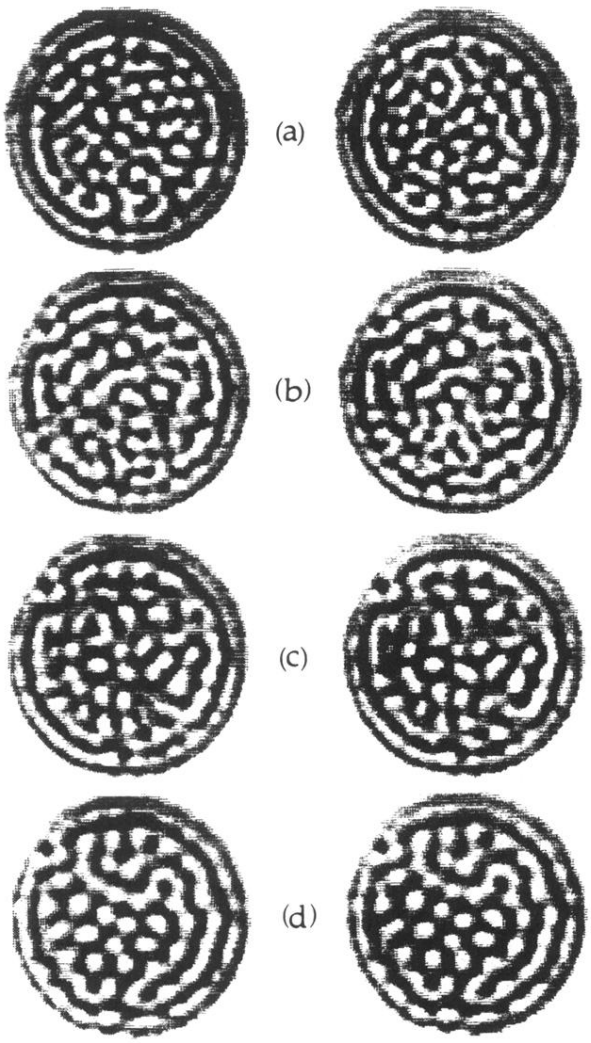

FIG. 26. Patterns observed during runs with $\delta \approx 2.0$ and $\epsilon_0 \approx 0.22$, and whose parameters are in the vicinity of the reproducibility/irreproducibility boundary. The images were taken on the (left) 69th and (right) 70th cycles. The frequencies are (a) $\omega = 8.0$, (b) 9.0, (c) 10.0, and (d) 12.0. For all cases $\epsilon_c \leq \epsilon_0 \leq \epsilon_R$.